Exploring characteristics for optimal accuracy of a settling sphere viscometer using the Lattice Boltzmann Method

by

W.M.A. Pols

Student number: 4171969
Project duration: September 1, 2015 – February 5, 2016
Thesis committee: Dr. M. Rohde, TU Delft, supervisor
Prof. J.L. Kloosterman, TU Delft

Summary

The world's demand for more and environment friendly energy ever increases. SAMOFAR, an international initiative of eleven institutions, responds to that demand by performing research to prove that a Molten Salt Fast Reactor (MSFR) is a safe option to produce energy. Among the research subjects is the design of a viscometer that can withstand the MSFR core's maximal temperature of 1100K.

In this thesis the Lattice Boltzmann Method (LBM) is used for a quantitative analysis of four properties of a falling sphere-like viscometer design: the density range between the sphere and the salt, the cross sectional area of the measurement vessel, the shape of the settling object and the detection height. The settling sphere method is applied by a permanent magnet that is released at the top of the vessel. Its magnetic field is then detected after a certain distance. The time the object takes to cover the distance is directly related to the viscosity.

The used LBM model contains the Bhatnagar-Gross-Krook relaxation parameter, a local grid refinement in the volume where the largest velocity and pressure gradients occur and an application of the halfway bounce-back method on both the stationary and the moving walls. The physical simulation volume is 1.2x1.2x2.0mm^3. A kinematic viscosity range of $0.7 \cdot 10^{-6} - 2.1 \cdot 10^{-6}\mathrm{m}^2/\mathrm{s}$ was explored.

Each of the four properties is varied around a common reference set of simulations in order to find which value results in the most accurate determination of the viscosity when a measurement uncertainty of 0.01s is applied on the settling time. It is generally shown that longer settling times enable more accurate viscosity measurements and that the absolute uncertainty range is larger for smaller viscosities.

The reference set shows an uncertainty range of $3.6\% - 1.1\%$ for $\nu = 0.7 \cdot 10^{-6}\mathrm{m}^2/\mathrm{s}$ and $\nu = 2.1 \cdot 10^{-6}\mathrm{m}^2/\mathrm{s}$ respectively. The strongest reduction was due to a decrease in the density ratio, namely $1.1\% - 0.4\%$. The cross sectional area reduction and a lower detection point both showed an uncertainty range of $2.8\% - 0.9\%$. The elongation of the settling sphere reduced the uncertainty ranges to $3.3\% - 1.0\%$.

This thesis functions as a first quantification of optimisation possibilities for a novel measurement technique for molten salt in the core of an MSFR. Multiple possible constraints, like the penetration of the magnetic field through the core's wall, still have to be assessed to analyse realisation potential of this method.

Contents

1 Introduction

1.1 Problem statement

Providing enough energy for the world population becomes an increasing challenge over time. Not only is the population expected to reach over 9.7 billion in 2050 [1], the effect on energy demand increases as energy consumption per capita will grow as well [2]. Because of this increasing demand and the worldwide concern for reducing CO_2 emissions, nuclear power comes forward as a promising solution for the energy problem. However, hesitations exist about the future of nuclear power, partly due to the Fukushima Daiichi power plan accident in 2011.

In 2000 six new types of Generation IV Nuclear Reactors were proposed by the Generation IV International Forum [3]. The primary goal for the proposals was the development of a way to produce nuclear energy in a truly safe way regarding sustainability, safety and reliability, proliferation resistance and physical protection. Furthermore, economic competitiveness is the last goal of the Generation IV Nuclear Reactors.

One of these proposed energy reactors is the Molten Salt Reactor (MSR). The Molten Salt Fast Reactor (MSFR) is one of the two MSR systems that are under consideration. This type of fast spectrum reactor uses thorium fluoride salt as its fuel and would operate near 1100K [4]. This temperature enables the fuel salt to melt and mix with other fluoride salts that act as the reactor's coolant, but at the same time, a temperature of 1100K stays far away from the boiling temperature of the salts. Due to these properties the process can run at low pressure [3].

The development of the Generation IV Nuclear Reactors is categorised in three phases: the viability phase, the performance phase and the demonstration phase. The MSR is expected to exceed the viability phase in 2025 [3].

SAMOFAR, an international initiative of eleven institutions, aims to 'deliver indisputable evidence of the excellent safety features of the MSFR' and to bring the MSFR to the demonstration phase. To reach this, SAMOFAR plans to explore and experiment with key safety features, such as draining of the fuel salt, new coatings and the dynamics of natural circulation.

Among the safety features, the measurement of safety-related data of the fuel salt is a research goal as well, as various physical properties need monitoring while the reactor runs. Due to the extreme environment the molten salts create, a specific set of measurement equipment is necessary. The devices must be robust enough to withstand temperatures up to 1100K.

The demonstration phase of the Generation IV Reactors is an engineering-scale process, in which prototypical conditions are created to verify physical phenomena and optimise material capabilities [3]. In the case of the MSFR, the test setup would consist of a FLiNaK

(LiF, NaF, KF) bath. FLiNaK is a eutectic composition and therefore has a relatively low melting point – as a reference, 46.5 mol% LiF, 11.5 mol% NaF, 42 mol% KF melts at 727K, while each of the individual salts melt at temperatures over 1100K [5]. Though FLiNaK is not the salt that will be used in the MSFR, the viscosity range used in this thesis is based on extrapolated data of the test salt, as its properties should not differ much from the fluoride salts in the reactor.

1.2 Measurement of viscosity in an MSFR

Apart from some types that separate a small volume to do measurements, most viscometers exist from an object that vibrates, rotates or translates in any way and a part that measures its movements. Either the force to keep the movement constant or the time a certain attenuation takes is used to base the viscosity measurement on [6]. Due to its high temperatures, the MSFR needs a more robust version of the viscometer. Still, the same principle can be used as proposed by Rohde [7]: an object with a density larger than the core will be released from the top of a certain experimental vessel and time it takes cover a certain distance can be measured. Ideally a set of calibration data would provide a direct relation between the measured time and the viscosity, when other properties like the salts' density and dimensions of the vessel are known.

The detection of the settling object would be problematic, as the measuring part of the viscometer probably would be unable to withstand the vessel's environment and therefore should be placed outside the vessel, disabling mechanical communication between the two parts of the viscometer. However, a magnetic field around the settling object could enable the communication through the core's walls. A cobalt object would be able to maintain a magnetic field, as its Curie temperature of 1388-1398K (in case of a hcp lattice) lies well above the operating temperature of the MSFR and its test setup [8].

The process of a settling object was simulated using Computational Fluid Dynamics (CFD). The Lattice Boltzmann Method (LBM) was used to investigate the effect of various values of four properties of the viscometer: the ratio between the fluid's density and the density of the settling object, the shape of the object, the cross sectional area of the vessel and the detection height. These features were varied to quantify the measurement precision of the viscosity and find the most desirable property values.

1.3 Lattice Boltzmann Method

LBM finds its roots in the Lattice Gas Automata (LGA), which is a type of CFD using a simple set of rules for moving particles in a grid. The first model, proposed by Hardy, de Pazzis and Pomeau, discretized a 2D fluid by applying a grid over which discrete particles could move – four directions from each node. The particles had one possible speed and their movements were managed by a set of advection and collision rules that employ the rules of mass and momentum conservation [9]. The model was improved by Frisch, Hasslacher and Pomeau by their proposal to create a grid of triangles instead of squares, allowing particles to advect in six directions [10]. The results were more promising but still showed noise. The solution was introduced by McNamara and Zanetti, by their idea to apply the Boltzmann equation on the LGA. This equation made it possible to manage real numbers instead of Booleans to describe

particle flows. They introduced mesoscopic probability density flows of particles that were subject to advection and colliding terms that still conserved mass and momentum conservation [11]. This proposal marked the start of LBM.

LBM still was a computationally demanding method to analyse fluid dynamics, and therefore a slow way to calculate setups in the desired resolution. Qian *et al*. found a solution to reduce the computational time by introducing the Bhatnagar-Gross-Krook method for lattice gasses to LBM. This replaces the numerically heavy collision operator of LBM, originally an operator that covered particle redistribution for every two directions particle densities were to come together, by a single relaxation parameter [12].

Computation time was further reduced by multiple suggestions for local grid refinement methods. Empirical measurements can identify large velocity gradients in fluids, thereby declaring high resolution requirements in certain parts of the setup. This local refinement allows the rest of the covered volume to be filled in by a coarser grid [13]. Refinement techniques are for example based on rescaling of particle velocities or interpolation of particle densities [14] [15]. The method that was used in this thesis was proposed by Rohde *et al.* and is based on temporal refinement of the coarse cells [16]. This second addition enables a detailed view within a large area within a reasonable time span.

1.4 Outline

This thesis consists of five parts. Chapter 2 will explain the underlying theory on the general LBM, along with some constraints that directly affect the choice of input parameters. Furthermore multiple features that are added to the original version of LBM are discussed. In chapter 3 the completion of the model is covered. Besides, this chapter will elaborate on the four explored properties of the viscometer and the data treatment to conclude measurement accuracy from the simulations. Chapter 4 includes the simulation data and further explain data handling, of which the outcomes will be elaborated on in chapter 5. Recommendations for further research are made in chapter 6.

2 Theory

2.1 Settling sphere

When a sphere is released in a fluid with infinite volume it will be subject to gravitational force, buoyancy and drag force. Assuming the density of the sphere is greater than the fluid's density, at first the gravitational force will be dominant, causing the sphere to accelerate downwards. Buoyancy and drag will then increase and thereby cause the acceleration to decrease until the sphere moves at constant velocity, i.e. its terminal velocity.

The problem that is described above can be solved analytically. However, if we eliminate the assumption of an infinite volume, but instead let the sphere settle in a fluid in a finite volume, it cannot. Brenner showed that a particle in a finite tank is affected by the side walls, even if those walls are infinitely far away from the particle [17]. It is remarkable though, that the presence of a bottom has a far smaller effect. Only when it approaches the bottom very closely, a settling sphere behaves very differently from the case of infinite depth [18]. However, in this thesis smaller deceleration effects are found earlier in the trajectory as well.

Thus, to describe the sphere's motion in a finite volume, a numerical analysis is necessary. The Lattice Boltzmann Method was chosen to do this simulation due to its relatively quick and accurate results and because solid boundaries are relatively easy to implement in into LBM models.

2.2 General LBM

The Lattice Boltzmann Method is a numerical approach to fluid dynamics that, in its nearly incompressible limit, is shown to approximate the incompressible Navier-Stokes equations [19]. This is further elaborated on in paragraph 2.2.3.

LBM is based on the idea that motion of microscopic particles defines the macroscopic behaviour of the fluid. This translation is made by a mesoscopic setup of the particle flow: the model describes multi-particle flows that move by advection and collision over a 2D or 3D grid that is applied on a certain area or volume.

LBM works fully discretised: each cell has its dimensions expressed in ls (lattice spacing) and every time step takes 1lt (lattice time step). Due to the discretisation, physical units in the model are expressed in ls and lt instead of m and s. For conversion the quantities S and T were introduced:

$$1\text{ls} = S\text{m}; \quad 1\text{lt} = T\text{s} \tag{1}$$

S has the units [m/ls] and T [s/lt]. This allows translation to the LBM for all quantities. For example, the sphere's velocity is conversed by $v^*T/S = v$ (in units: [m/s][s/lt][ls/m] = [ls/lt], so v^* is expressed in [m/s] and v in [ls/lt]). To avoid confusion, from now on physical quantities expressed in meters and seconds will be referred to by symbols with an asterisk (*).

All particles that exist within the volume of one cell are grouped in its center node. Each particle is assigned with a discrete velocity that allows it either to move to the node of an adjacent cell within one discretised time step, or stay on the same node, i.e. with zero velocity. The case of a so-called D2Q9 setup is shown in Figure 1: a 2D grid with nine possible velocities. In this thesis a D3Q19 model is used.

Particles are fully described by these two properties: the location of their cell $\vec{x}$ at time t, and their velocity $\vec{c}_i$. Furthermore, instead of individual particles, particle density distributions are simulated, as proposed by McNamara and Zanetti [11]. This creates a mesoscopic environment that allows LBM's celebrated quickness and accuracy.

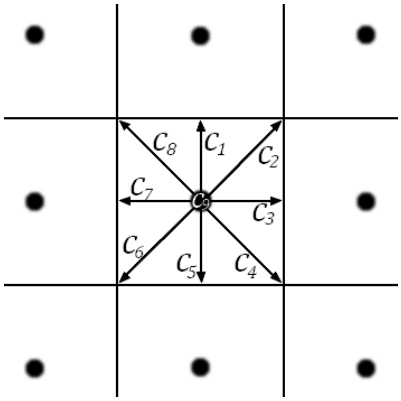

Figure 1. In LBM of the D2Q9, particle densities have nine possible velocities. They can move in eight directions ($c_1 \dots c_8$) to its eight adjacent cells or have zero velocity (c_9). In three dimensions D3Q15 and D3Q19 methods exist.

Each propagation step contains two separate actions: a advection process and a collision step that redistributes the particle densities' velocities. The particle density f_i ($i = 1 \dots Q$, where Q is the number of directions that the particles can travel) as proposed by McNamara and Zanetti is represented as follows:

$$f_i(\vec{x} + \vec{c}_i \Delta t, t + \Delta t) = f_i(\vec{x}, t) + \Omega_i\big(f(\vec{x}, t)\big) \qquad (2)$$

The streaming step allows a particle density f_i at location $\vec{x}$ and time t to travel a distance of $\vec{c}_i \Delta x$ within Δt, where $|\vec{c}_i| = \Delta x / \Delta t$. Following the model's discretisation, generally $\Delta x = 1$ls and $\Delta t = 1$lt. However, local grid refinement allows other values, as described in paragraph 2.3.

The collision step is represented by $\Omega_i\big(f(\vec{x}, t)\big)$, an operator that expresses the change in f_i due to collision. This operator describes the scattering rate between every combination of two particle densities that flow from different directions to meet in a node. Moreover, it provides conservation of mass and momentum in the lattice. As the original operator appeared very demanding regarding computational time it is often replaced by the Bhatnagar-Gross-Krook collision term. The BGK method replaces $\Omega_i\big(f(\vec{x}, t)\big)$ so the LBGK equation is obtained [12]:

$$f_i(\vec{x} + \vec{c}_i\Delta t, t + \Delta t) = f_i(\vec{x}, t) - \frac{f_i - f_i^{eq}}{\tau} \quad (3)$$

Here $\tau = 1/\omega$ where ω is the singe relaxation term. The relaxation time τ is directly related to the kinematic viscosity ν in LBM-units:

$$\nu = 1/3(\tau - 1/2) \quad (4)$$

Next, the term f_i^{eq} in equation (3) comes forward in the formal expansion of f_i about the local equilibrium distribution function:

$$f_i = f_i^{eq} + \epsilon f_i^{(neq)} \quad (5)$$

f_i^{eq} represents the local equilibrium distribution function, while $f_i^{(neq)}$ is its counterpart, the nonequilibrium distribution function. Here ϵ is of a magnitude in the order of S and T.

In case of an applied body force $\vec{g}$, due to gravity, another term has to be added in equation (3). The expanded equation reads

$$\boldsymbol{f_i}(\vec{\boldsymbol{x}} + \vec{\boldsymbol{c}}_i\Delta \boldsymbol{t}, \boldsymbol{t} + \Delta \boldsymbol{t}) = \boldsymbol{f_i}(\vec{\boldsymbol{x}}, \boldsymbol{t}) - \frac{\boldsymbol{f_i} - \boldsymbol{f_i^{eq}}}{\boldsymbol{\tau}} + \boldsymbol{t_{f,i}\rho_l}(\vec{\boldsymbol{c}}_i \cdot \vec{\boldsymbol{g}}) \quad (6)$$

There $\boldsymbol{\rho_l}$ is the fluid's density and $t_{f,i}$ is a scaling factor that depends on the type of LBM and $\vec{c}_i$ [12]. In case of D3Q19,

$$t_{f,i} = \begin{cases} \frac{12}{36} : \vec{c}_i = (0,0,0) \\ \frac{2}{36} : \vec{c}_i = (\pm 1,0,0), (0 \ \pm 1,0), (0,0 \pm 1) \\ \frac{1}{36} : \vec{c}_i = (\pm 1, \pm 1,0,)(0, \pm 1, \pm 1), (\pm 1,0, \pm 1) \end{cases}$$

Equation (4) introduces ν, a representation of kinematic viscosity expressed in [ls^2/lt]. This enables direct use of the value in the LBM model. Conversion is done by $\nu = (T/S^2)\nu^*$. Furthermore, $\vec{g}^*$ [m/s^2] , the body force due to gravity, has an LBM equivalent $\vec{g}$ [ls/lt^2].

However, the fluid's density (ρ_l^*) and its momentum density ($\rho_l^*\vec{u}^*$) do not have a direct conversion to LBM equivalents like ν and $\vec{g}$. They are defined as discrete sums of the particle distribution functions:

$$\rho_l = \sum_{i=1}^{Q} f_i \,; \ \ (\rho_l \vec{u}) = \sum_{i=1}^{Q} f_i \vec{c}_i \quad (7)$$

2.2.1 Stokes flow

As the model is meant to create an environment to measure viscosity precisely, the effect of advective forces should be smaller than viscous forces, which means Stokes flow simulations provide the most accurate results. To maintain Stokes flow, the model should generally obey that Re $\ll 1$. Simulations by Rohde *et al.* [13] of a settling sphere of $D = 8$ls in a range of Reynolds numbers of 0.1 to 1.0 showed that no significant change in drag force occurred for $Re^* < 0.5$. Hence, a Reynolds number of 0.5 is small enough to simulate a flow in the Stokes regime.

2.2.2 Kinematic viscosity value in LBM

Like every numerical method, LBM shows an error due to various properties of the model. The error due to the halfway bounce-back boundary condition, that applies on fluid velocity $\vec{u}_i$ at node k at height z_k, was found by He *et al.* [20] and expanded with a second term by Rohde *et al*. [21]. This equation was originally derived for the error in channel flow simulations, but it was also shown to be a close approximation for the error in the flow around a sphere by Rohde.

$$\Delta u_i(z_k) = \frac{U_{max}\left(16\tau^2 - 20\tau + 3\right)}{3L^2} + \frac{4U_{max}\alpha(\alpha-1)}{L^2} \qquad (8)$$

Here U_{max} is the maximum velocity of a Poiseuille flow profile and L is the height of the channel. α represents the volume fraction of a cell at the boundary. In case of the walls where the halfway bounce-back method is applied, $\alpha = 1$, as the boundary lies exactly between two nodes, so the second term of equation (8) becomes 0. In case of a differently shaped wall, for example a settling discretised sphere, α has different values.

$\Delta u_x(z_k)$ can actually approach zero, as $16\tau^2 - 20\tau + 3 = 0$ for $\tau = \left(5 \pm \sqrt{13}\right)/8$. The smaller of the two solutions is not to be used as equation (4) shows that this value for τ it would create a negative ν. Therefore the model is optimised for $\nu = (1 + \sqrt{13})/24 \mathrm{ls}^2/\mathrm{lt}$.

2.2.3 Mach number

LBM converges to the compressible, isothermal Navier-Stokes equations [22]:

$$\partial_t \rho_l^* + \nabla \cdot (\rho_l^* \vec{u}^*) = 0 \qquad (9)$$

$$\partial_t (\rho_l^* \vec{u}^*) + \nabla \cdot \left((\rho_l^* \vec{u}^* \vec{u}^*) + c_s^{*2} \rho_l^* \mathrm{I}\right) = \nabla \cdot \mathrm{S}^* + O(\mathrm{Ma}^{*3}/\mathrm{Re}) \qquad (10)$$

In these equations, $c_s^{*2}\rho_l^*$ is the pressure, I is the identity tensor and S^* is the viscous stress tensor. Furthermore, $\vec{u}^*$ is the macroscopic velocity of the fluid, and c_s^{*2} is the speed of sound in the fluid. Finally, the term $O(\mathrm{Ma}^{*3}/\mathrm{Re})$ represents compressibility, thus by stating the Mach number $\mathrm{Ma}^* \ll 1$, the Navier-Stokes equations are solved in the incompressible limit, where ρ_l^* is constant [22]. (Although the Mach number is a dimensionless number, an asterisk is added because an LB-version will be introduced later in this thesis.)

For small Ma^*, the incompressible Navier-Stokes equation is solved, with an error proportional to Ma^{*2} [22]. As the event that is simulated happens in the incompressible limit, it is necessary to work with these values where $\mathrm{Ma}^* \ll 1$ so the error is minimal. Generally values that obey $\mathrm{Ma}^* < 0.07$ are used.

$$\mathrm{Ma}^* = \frac{|\vec{u}^*|}{c_s^{*2}} \qquad (11)$$

As the $|\vec{u}^*|$ that is to be found in the fluid will lay far from the speed of sound in a liquid, this constraint is accomplished easily.

However, the model has another constraint regarding maximum velocity: the sphere may only move a distance much smaller than Δx per Δt to be simulated correctly by the model. To

set this constraint, another interpretation of the Mach number can be used. An LB-equivalent of the number would be

$$\mathrm{Ma} = \frac{|\vec{v}|}{c_s} \qquad (12)$$

Here $\vec{v}$ represents the sphere's velocity and c_s is the speed of sound in LBM. When $\mathrm{Ma}^* \ll 1$ is obeyed, the fluid can be considered to be incompressible, thereby stating that compressions with the speed of sound can be ignored. As the speed of sound no longer matters, its value in LBM, c_s, becomes a tuneable quantity. However, for a 3D model with $Q = 19$, generally $c_s = 1/\sqrt{3}$ is used [23]. If the $\mathrm{Ma} < 0.07$ constraint is kept, like for Ma^*, $|\vec{v}| < 0.04\mathrm{ls/lt}$ is stated. This prevents the sphere from moving more than $0.07\Delta x$ in 1 Δt.

2.3 Local grid refinement

McNamara and Zanetti originally proposed a homogenous, Carthesian grid. However, the Lattice Boltzmann equation does not require a pre-fixed geometry: neither Carthesian coordinates nor equality of each cell are key conditions. The equation allows other discretisations of the simulated volume, which opens new possibilities regarding computational time reduction.

In areas where particle velocity gradients are high, a very fine grid is necessary to capture these gradients accurately enough. This results in a large amount of cells, requiring large computation times. To reduce the number of nodes, various proposals were made to vary the cells' dimensions. On volumes that are expected to carry high velocity gradients a finer grid can be applied. This obviously is a large reduction of nodes relative to a full coverage of the fine grid. The local refinement model used in this thesis was proposed by Rohde *et al.* [16], and uses rescaling factors to recalculate conversion constants S and T. As two cell sizes are used, rescaling introduces S_f for the fine grid and S_c for the coarse one, and T_f and T_c respectively. A rescaling factor $n = 2$ is used.

$$S_c = nS_f; \;\; T_c = nT_f \qquad (13)$$

In this refinement method, fine cells are considered 'normal', so $S_f = S, T_f = T$ and therefore $S_f\mathrm{m} = 1\mathrm{ls}$ and $T_f\mathrm{m} = 1\mathrm{lt}$. This means that fine cells have a volume of $1\mathrm{ls}^3$, and coarse cells, having edges of $2\mathrm{ls} = 1\mathrm{m}/S_c$, have the volume equal to eight fine cells. As $\vec{c}_i$ remains constant, particles can pass a fine cell in 1lt, but need $2\mathrm{lt} = 1\mathrm{s}/T_c$ to pass a coarse cell.

Furthermore, ν and $|\vec{g}\,|$ are to be converted as well for in the coarse grid. Due to the new quantity ν_c, τ_c is introduced as in equation (4). Due to all different values, viscosity and body force are applied on the two grid types separately.

$$\nu^* = (T_f/S_f^2)\,\nu_f = (T_c/S_c^2)\,\nu_c = (nT_f/n^2S_f^2)\,\nu_c \qquad \rightarrow \frac{1}{n}\nu_c = \nu_f = \nu$$

$$|\vec{g}^*| = (T_f^2/S_f)\,|\vec{g}_f| = (T_c^2/S_c)\,|\vec{g}_c| = (n^2T_f^2/nS_f)\,|\vec{g}_c| \;\rightarrow n|\vec{g}_c| = |\vec{g}_f| = |\vec{g}|$$

The grid refinement algorithm exists of five steps.

- First, the collision part of LBM is applied on both grids separately, as they do not interact yet.
- After that particles from each coarse cell are redistributed to eight cells of the size of the fine grid.
- This allows the third step, the convection part, to happen because particles can flow between the two grid types without constraints.
- Afterwards, as $T_c = 2T_f$, the particles in the fine grid undergo the collision step again, leaving the particles that are to enter the coarse grid untouched. Then again the streaming step is repeated for both grids.
- After that, the particle densities in the virtual smaller cells within the coarse grid are summed.

2.4 Halfway bounce-back method

2.4.1 Straight, stationary walls

General LBM allows various methods to describe the lattice's boundaries. In this research no-slip walls are used, by imposing the halfway bounce-back method. This method works as if there is one more layer of grid cells beyond the boundary of the lattice. These cells mirror the activities of the outer nodes within the lattice: they send back the exact particle flow they receive from the lattice, but with the opposite velocity.

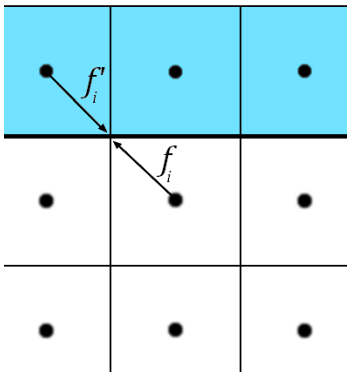

Figure 2. The grey cells represent the row of adjacent phantom cells, sending a mirrored f_i' back when f_i flows from a boundary cell inside the lattice. Here $|f_i| = |f_i'|$.

This tweak causes the particle velocity at the boundary to be zero in every direction and thereby meet the no-slip requirement.

2.4.2 Discretely curved walls

The object that is to settle in the simulation is generally a arbitrarily shaped wall that is able to move through the fluid: the walls influence the particles' flow and vice versa. The no-slip halfway bounce-back method applies on this wall as well.

The object is discretised in a way that allows its resolution to be finer than that of the grid which it is to be placed in: it is a set of coordinates that are grouped in triplets, forming triangular facets. Each coordinate is part of six triangles, and the triangles form a closed representation of the object. For each facet the normal unit vector, $\vec{n}^{\phi}$ is calculated, as well as

its surface area A^{ϕ}, where ϕ represents the facet. The object's coordinates are grouped in a way that creates only $\vec{n}^{\phi}$ that point outwards of the object.

The calculations for interaction with a stationary stairs-like wall of which the boundaries coincide with the cell borders of the grid was introduced by Chen *et al.* [24]. An extension allowing other geometries as well was later proposed by Rohde *et al*. [13]. Particles from cells adjacent to the object can flow with velocity $\vec{c}_i$ so that they are to interact with the object's wall. When the particles hit the wall with velocity $\vec{c}_i$, they are bounced back at $-\vec{c}_i$. To calculate the amount of particles that will collide, $P_i^{dist}(\vec{x})$ is introduced, which represents the amount of particles with velocity $\vec{c}_i$ that are to interact with the wall. Here $\vec{x}$ is the cell from which the particles flow. The share of particles that are to collide is given by

$$P_i^{dist}(\vec{x}) = \sum_{\phi} \frac{V_i^{\phi}(\vec{x})}{\Delta V(\vec{x})} \qquad (14)$$

where $V_i^{\phi}(\vec{x})$ is the volume of the cell that lies within $\vec{c}_i\Delta t$ of the wall facet ϕ, and $\Delta V(\vec{x})$ the total volume of the cell, minus the possible volume that is occupied by the object within that cell. One cell may lie within a distance of $\vec{c}_i\Delta t$ of multiple facets. As a matter of fact, the particles that are to interact with the wall all lie in a parallelepiped extruded from the facet up to a distance of $|\vec{c}_i|\Delta t$ in the opposite direction of $\vec{c}_i$. These parallelepipeds have a volume of $\Psi_i^{\phi} = \left|\vec{c}_i \cdot \vec{n}^{\phi}\right| A^{\phi}\Delta t$.

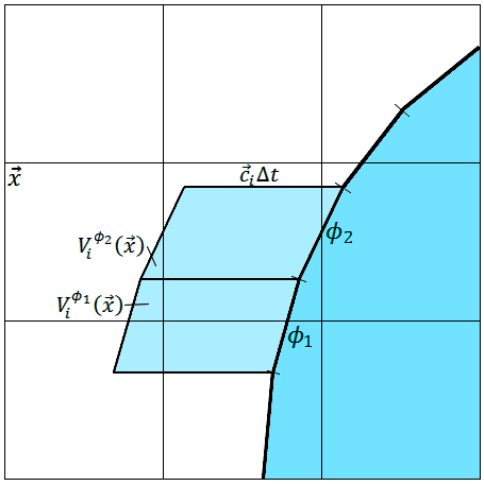

Figure 3. A representation of the bounce-back method around a discretised object (marked with dark grey). Only one direction $\vec{c}_i$ is elaborated on in this figure. The parallelepipeds that are extruded from two facets are marked light blue. The volumes of cell $\vec{x}$ that lie within $\vec{c}_i\Delta t$ from facets ϕ_1 and ϕ_2 represent $P_i^{dist}(\vec{x})$.

The adjusted equation for LBM now is

$$f_i(\vec{x} + \vec{c}_i\Delta t, t + \Delta t) = P_i^{undist}(\vec{x})\tilde{f}_i(\vec{x}, t) + Q_i(\vec{x} + \vec{c}_i\Delta t, t) \qquad (15)$$

In this equation P_i^{undist} is the undisturbed part of the particles that flow in the i-direction, so $P_i^{undist} = 1 - P_i^{dist}(\vec{x})$. $\tilde{\boldsymbol{f}}_{\boldsymbol{i}}(\vec{x}, t)$ represents the right part of normally used equation (6), i.e.

$f_i(\vec{x}+\vec{c}_i\Delta t, t+\Delta t) = f_i(\vec{x},t) - \frac{f_i - f_i^{eq}}{\tau} + t_{f,i}\rho_l(\vec{c}_i \cdot \vec{g})$. This leaves $Q_i(\vec{x}+\vec{c}_i\Delta t, t)$ to be the mass that is reflected by the object.

$$Q_i(\vec{x}+\vec{c}_i\Delta t, t) = \sum_\phi \frac{V_i^\phi(\vec{x}+\vec{c}_i\Delta t)}{\Psi_i^\phi}\Gamma_i^{out,\phi}(t) \qquad (16)$$

In this equation $\Gamma_i^{out,\phi}(t)$ represents the particle flow, originally with velocity $\vec{c}_i$, that is reflected from facet ϕ.

2.4.3 Moving discretely curved walls

Equation (15) applies to the case of a stationary object. If the object moves at velocity $\vec{v}(t)$ however, another term is to be added:

$$f_i(\vec{x}+\vec{c}_i\Delta t, t_*) = P_i^{undist}(\vec{x})f_i'(\vec{x},t) + Q_i(\vec{x}+\vec{c}_i\Delta t, t) + B_i(\vec{x}+\vec{c}_i\Delta t, t) \qquad (17)$$

Here t_* represents the moment before the wall moves. This new B_i-term introduces additional particle flux that is transferred from boundary cells within the object to the adjacent fluid cells in case that $\vec{c}_i \cdot \vec{v}(t) < 0$ and transferred the other way when $\vec{c}_i \cdot \vec{v}(t) > 0$. Over the total volume, mass is therefore conserved, while momentum is transferred to the bottom of the descending object. This transferred mass is in this case

$$\Delta\Gamma_i^{out,\phi}(\vec{x},t) = 2t_{f,i}\frac{V_i^\phi(\vec{x},t)}{\Delta V(\vec{x},t)}M(\vec{x},t)(\vec{v}(t)\cdot\vec{c}_i)/c_s^2 \qquad (18)$$

Here $t_{f,i}$ is the same weight factor as used in equation (6). $M(\vec{x},t)$ is the total mass in cell $\vec{x}$ at time t, depending on $\widetilde{M}(\vec{x},t)$, the total mass in the cell without the addition of the B_i-term:

$$M(\vec{x},t) = \frac{\widetilde{M}(\vec{x},t)}{1-2\sum_\phi\sum_{i\in\vec{c}_i\cdot\vec{n}^\phi(t)>0}\left\{V_i^\phi(\vec{x},t)\right\}/\left\{\Delta V(\vec{x},t)t_{f,i}(\vec{v}(t)\cdot\vec{c}_i)/c_s^2\right\}} \qquad (19)$$

Now $\Delta\Gamma_i^{out,\phi}(\vec{x},t)$ is fully expressed, it is possible to write $B_i(\vec{x}+\vec{c}_i\Delta t, t)$ in terms of it:

$$B_i(\vec{x}+\vec{c}_i\Delta t, t) = \sum_\phi \Delta\Gamma_i^{out,\phi}(\vec{x}+\vec{c}_i\Delta t, t) \qquad (20)$$

In the model the flow near this descending object can be simulated following five steps

- First, quantities that follow directly from the stationary geometry should be calculated: $\Delta V(\vec{x},t), \Psi_i^\phi(t), V_i^\phi(\vec{x},t)$ and $\vec{n}^\phi(t)$.
- The flow field for a fixed wall can now be calculated as described in equation (15), but now for $t = t_*$.
- Now B_i can be added: $f_i(\vec{x}+\vec{c}_i\Delta t, t_*)$ is calculated from equation (17).
- Next, the object is moved over a distance of $\vec{v}(t)\Delta t$.
- Now $f_i(\vec{x}+\vec{c}_i\Delta t, t+\Delta t)$ can be calculated.

N.B. this model only allows translational motion for the object, hence rotational motion is not included here.

2.5 Hydraulic diameter of the object

The simulated shear stress on the settling object shows an offset due to the model's formulation of the shear stress. This deviation is unphysically dependent on the used value of ν and can be corrected for by a slight rescaling of the object. This rescaling is realised by introducing the hydraulic diameter, D_{hydr} [13] that deviates slightly from the diameter of the object, D.

To determine the value of D_{hydr}, multiple simulations with various values of ν must be executed. The simulated drag force and analytical drag force values, as derived by Hasimoto [25], can be compared. Rohde *et al.* [26] showed that for small values of ν, like $\nu \sim 1/96$, the drag force in the simulation is larger than the analytically found one, while simulated drag force appears smaller than analytical values for large ν ($\nu \sim 2/3$). The simulated and the analytical solutions meet near the value of $\nu = 1/6 \mathrm{ls}^2/\mathrm{lt}$, which lies close to $\nu = (1 + \sqrt{13})/24 \mathrm{ls}^2/\mathrm{lt}$.

D_{hydr} corrects for drag force deviations between simulations and analytically found values. The case of $D_{hydr} < D$ corrects for small ν and $D_{hydr} > D$ for large values of ν.

3 Methodology

3.1 LBM model

3.1.1 General setup

In each of the simulations the fluid volume is simulated by a cuboid with two grid types: a fine one with cell edges of 1ls and the coarse grid with edges of 2ls. The fine grid is implemented in the center of the lattice, where Ten Cate *et al.* [27] showed the largest velocity gradients to occur. A volume of $16 \times 16 \times 100$ ls^3 is applied. It is surrounded by a 22ls thick layer of the coarse grid, creating a total cuboid volume of $L_x \times L_y \times L_z = 60 \times 60 \times 100$ ls^3. The thickness of the coarse layer is only varied when exploring the effect of different volume sizes as explained in paragraph 3.3.2.

Ten Cate *et al*. [27] performed viscosity measurements with a silicone oil in which a Nylon sphere was released. It was found that the highest velocity gradients occur within a cross sectional area of $2D \times 2D$ in the center of the vessel [27]. In this simulation the fine grid therefore roughly covers the volume up to a distance of $D/2$ from the sphere.

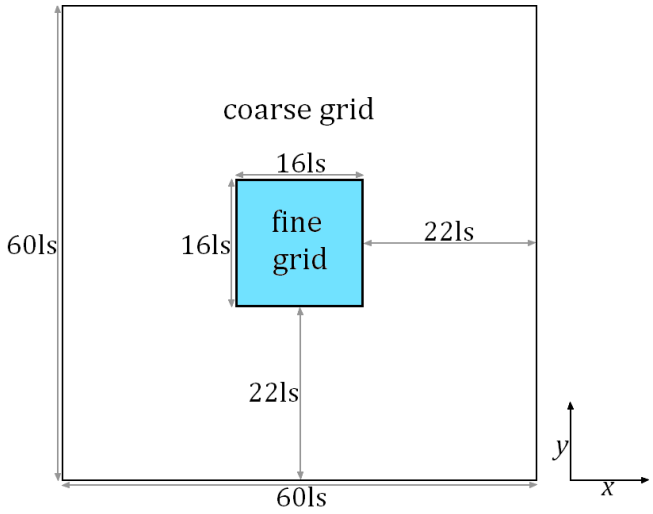

Figure 4. The top view of the lattice. Simulations were performed on a 100ls high cuboid.

The settling object is, apart from the simulations that varies the shape 3.3.3, the same as the one used by Rohde *et al.*: a discretised sphere, consisting of 176 triangular faces of which each corner is represented by a coordinate [26]. The coordinates that make up the sphere obey $D = 9$ls. However, due to the discretisation process the surface area of the sphere becomes smaller, as shown in the case of a circle in Figure 5. Therefore a slightly larger geometrical diameter is introduced, that causes the area of the object to resemble that of a sphere with $D = 9$ls more accurately. Every coordinate is multiplied by a factor D_{geom}/D. In Rohde's 176-faced object, $D_{geom} = 9.16$ls was used, and that value will be re-used for the same sphere in this thesis.

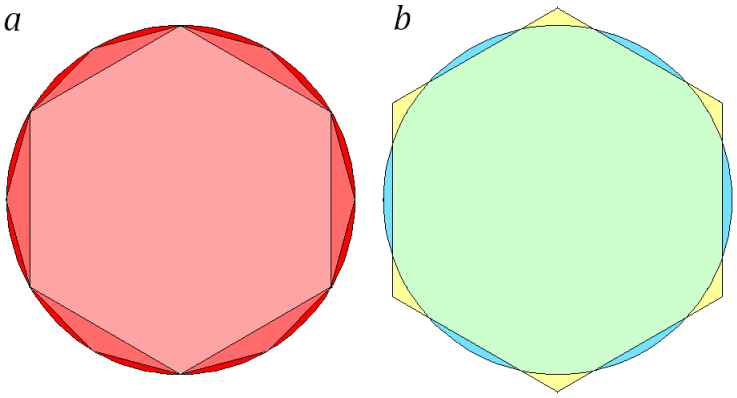

Figure 5. a. The periphery of a discrete approximation of a circle with the same diameter mismatches that of the real circle. The larger the amount of faces, the better the approximation. b. If the diameter of the discrete figure is slightly larger, the periphery becomes a better approximation

Furthermore, this sphere is assigned with a hydraulic diameter of $D_{hydr} = 9.027\text{ls}$, as it had in Rohde's experiments. As explained in paragraph 2.5, D_{hydr} is a correction factor that reduces the difference between the simulated drag force and analytically found values of that force. The deviation of simulated shear stress depends on ν in an unphysical way, so D_{hydr} is dependent on ν. Though Rohde used $\nu = 1/6\ \text{ls}^2/\text{lt}$ and this thesis uses $\nu = (1+\sqrt{13})/24$, $D_{hydr} = 9.027\text{ls}$ remains a close enough approximation.

For each calculation the sphere's center is placed in the center of the cuboid as seen from the top, at $h_0 = 80\text{ls}$ ($h = 0\text{ls}$ being the bottom of the vessel). The object is released at $t = 0\text{lt}$ and from then subject to the gravitational force $\vec{g}$. After every time step of 1lt its position coordinates and the three gradients are saved.

The object is detected when its center passes $h_d = 40\text{ls}$, except for the simulations that examine the influence of different detection heights, as elaborated on in paragraph 3.3.4. This height is sufficiently far away from the bottom to avoid major bottom effects, as those only appear about 1ls above the bottom [18].

3.1.2 Determination of quantities in LBM

3.1.2.1 Viscosity

As an LBM model uses the LB-units ls and lt, an LB-version of the kinematic viscosity is necessary. As shown in paragraph 2.2.1, $\nu = (1+\sqrt{13})/24\text{ls}^2/\text{lt} \approx 0.19\text{ls}^2/\text{lt}$ reduces the error in fluid velocity that is induced by the halfway bounce-back method.

An analysis of the effect of using a different value for ν is made before fixing values of S and T for the actual simulations. Therefore, a set of test runs is performed. Because the effect of varying ν is explored, all other properties must remain constant. Therefore each run simulates the same sphere settling in the same volume of a fluid with the same viscosity $\nu^* = 5.0 \cdot 10^{-4}\text{m}^2/\text{s}$. The special conversion factor is fixed as well: $S = 2.0 \cdot 10^{-3}\text{m/ls}$. Obviously, the LB-viscosity, ν, is varied. Now ν^*, S and a range of ν-values are set, T is a result of those, as $T = S^2\nu^*/\nu$. The variables for each run are shown in Table 1. For all combinations, $\text{Ma} < 0.07$.

Table 1.Measurement values setup for Figure 6. To explore the effect of a varied ν, ν^* and S are kept constant. A range of ν was chosen, and T was used to fit the other three quantities together.

$\boldsymbol{\nu^*}\ [\mathbf{m^2/s}]$ $\times \mathbf{10^{-4}}$	S [m/ls] $\times 10^{-3}$	T [s/ts] $\times 10^{-3}$	ν [ls^2/lt]
5.00	2.00	1.60	0.20
5.00	2.00	1.33	0.17
5.00	2.00	1.00	0.13
5.00	2.00	0.80	0.10
5.00	2.00	0.40	0.05

Simulations with the sphere with $D \approx 9$ls are run from $h_0 = 80$ls in the $60 \times 60 \times 100$ ls^3 lattice. D_{hydr} depends on ν: it should decrease when ν increases and vice versa. However, as determination of D_{hydr} was not available for other values of ν it was kept constant at $D_{hydr} = 9.027$ls, while it should increase slightly as ν decreases. Figure 6 clearly shows that a varying ν has a heavy effect on the velocity v^* of the sphere, even though the same physical problem is solved for every run. Because the other values create a significant offset $\nu = 0.19$ls^2/lt is kept constant for all further simulations.

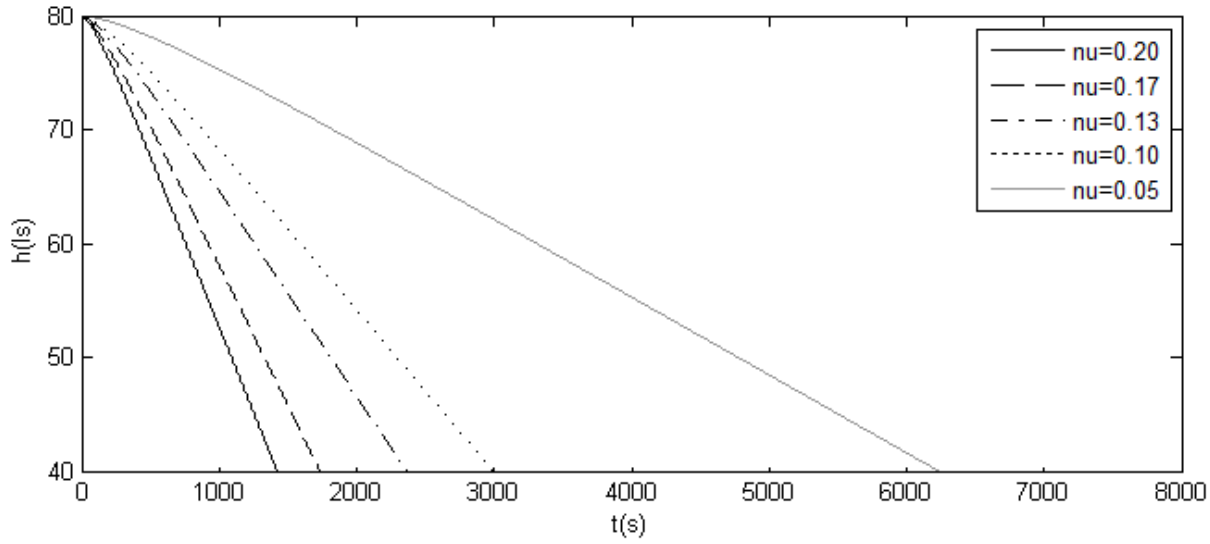

Figure 6. The height of the settling sphere with various ν values, while ν^* was kept constant. Values of t are multiplied by the scaling factor T to express t^* in seconds.

Now that ν is fixed, a range of ν^* is chosen for the simulations. This range is based on extrapolated data of Janz *et al.* [5] on the dynamic viscosity and density of FLiNaK. A temperature range of $850 - 1100$K roughly corresponds to a kinematic viscosity range of $6 \cdot 10^{-7} - 2.2 \cdot 10^{-6}$m^2/s [28]. Intervals of $2 \cdot 10^{-7}$m^2/s are chosen to observe the viscosity's effects on settling time.

3.1.2.2 Lattice space and lattice time

With a value for ν fixed and a range for ν^* set, the conversion factors S and T can be determined. Because the simulation sets are meant to vary one property (i.e. density ratio, cross sectional area, object shape or detection height), other physical properties are to be kept constant throughout the runs, the volume of the vessel being one of those. To maintain a

constant volume, S and volume $L_x \times L_y \times L_z = 60 \times 60 \times 100\ \mathrm{ls}^3$ are chosen to be invariable. This leaves T to be determined as a result of ν^*, ν and S, because $T = S^2\nu^*/\nu$.

S and T cannot be chosen arbitrarily, as the model has to meet the constraint of $\mathrm{Ma} = \sqrt{3}|\vec{v}| < 0.07$. To explore the constraint the terminal velocity $\vec{v}^*_{term}$ of a sphere moving with constant velocity in an infinite medium is calculated for each value of the ν^*-set. Then a value for S is chosen that allows $\vec{v}^*_{term}$ for each value of ν^* to be converted to a small enough $\vec{v}$ to fit the Mach constraint. That value is $S = 2.0 \cdot 10^{-5}\mathrm{m/ls}$. Table 2 shows the resulting T-range and values for $|\vec{g}|$.

The choice for this value of S means that the physical volume of the simulation is $1.2 \times 1.2 \times 2.0\ \mathrm{mm}^3$. This seems unrealistically small, but the model can be scaled up as long as the Reynolds number remains the same.

Table 2. To maintain a constant volume, S is constant. T is then a result of ν, ν^* and S. The Ma constraint is met for each data set. The used body force is calculated in the last column.

$\boldsymbol{\nu}\ [\mathbf{m^2/s}]$ $\times \mathbf{10^{-7}}$	S [m] $\times 10^{-5}$	T [s] $\times 10^{-5}$	Ma $\times 10^{-2}$	$\lvert\vec{g}\rvert$ [ls/lt^2] $\times 10^{-2}$
6.00	2.00	12.8	4.63	0.803
8.00	2.00	9.59	2.46	0.452
10.0	2.00	7.68	1.96	0.289
12.0	2.00	6.40	1.64	0.201
14.0	2.00	5.48	1.40	0.147
16.0	2.00	4.80	1.23	0.113
18.0	2.00	4.26	1.09	0.089
20.0	2.00	3.84	0.98	0.072
22.0	2.00	3.49	0.89	0.060

3.2 Data analysis

3.2.1 Height and velocity of the sphere

Each simulation results in the position of the center of the sphere in three dimensions and its velocity in three directions (i.e. $\vec{v}(t) = (v_x, v_y, v_z)$) at each time step. An example of a simulation is given in Figure 7, where the sphere's height and velocity are plotted against time. This simulation corresponds to the first case that is described by Table 2, i.e. $\nu^* = 6.00 \cdot 10^{-7}\mathrm{m}^2/\mathrm{s}$, $S = 2.00 \cdot 10^{-5}\mathrm{m/ls}$, $T = 12.8 \cdot 10^{-5}\mathrm{s/lt}$ and $|\vec{g}| = 0.803 \cdot 10^{-2}\mathrm{ls/lt}^2$. The density ratio $\frac{\rho_s}{\rho_l} = 1.15$ (ρ_s represents the density of the settling object), the settling object was a sphere and the cross sectional area $60 \times 60\mathrm{ls}^2$.

The height of the sphere in graph (a) shows an acceleration in roughly the first 1000lt. Then a period of constant velocity follows, continued by a deceleration. The model stops when the sphere's center is 4.60ls from the bottom.

The velocity profile (b) shows the same: acceleration after release and deceleration as the sphere approaches the bottom. However, a peak near $h = 4.60\mathrm{ls}$ shows an extreme activity

just before the sphere hits the bottom. This peak is due to the very high pressure and velocity gradients when the sphere approaches the bottom, which are not calculated accurately with the current resolution. This problem could be solved by refining the grid just above the bottom, but as the model works well for the heights that are relevant for the viscometer, further refining was not necessary.

The last graph of Figure 7 shows that the velocity, and thus the displacement of the sphere in the x and y directions, is noisy and much smaller than the motion in the z direction. Though the x gradient seems to show a certain shape, its magnitude is negligible compared to the velocity in the z direction. Therefore these movements can be considered insignificant and are thus ignored.

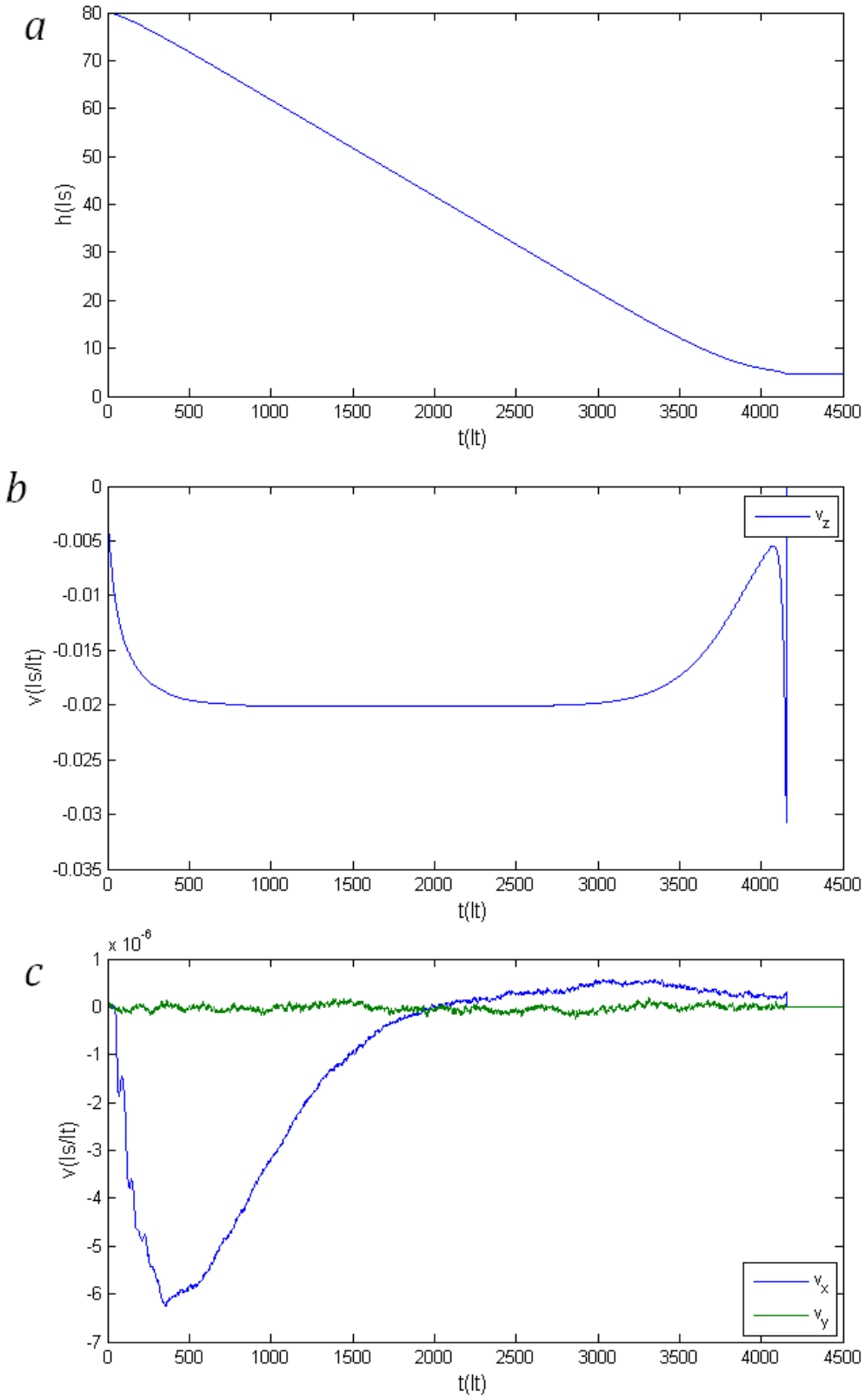

Figure 7. The direct output of a LBM simulation, where $\nu^* = 6.00\mathrm{m}^2/\mathrm{s}$, in a $60 \times 60 \times 100\mathrm{ls}^3$ grid with a regular discrete sphere, while $\rho_s/\rho_l = 1.15$. a. The height of the center of the sphere over time. b. The velocity in the z direction over time. c. The velocities in x and y direction over time.

3.2.2 Measurement accuracy

Figure 8 shows the heights over time of three simulations. From each simulation one quantity is recorded for further analysis: the past time Δt_d^* between the release of the sphere at h_0 and the detection at $h_d = 40\text{ls}$. The values of Δt_d^* are marked by the dotted lines in Figure 8.

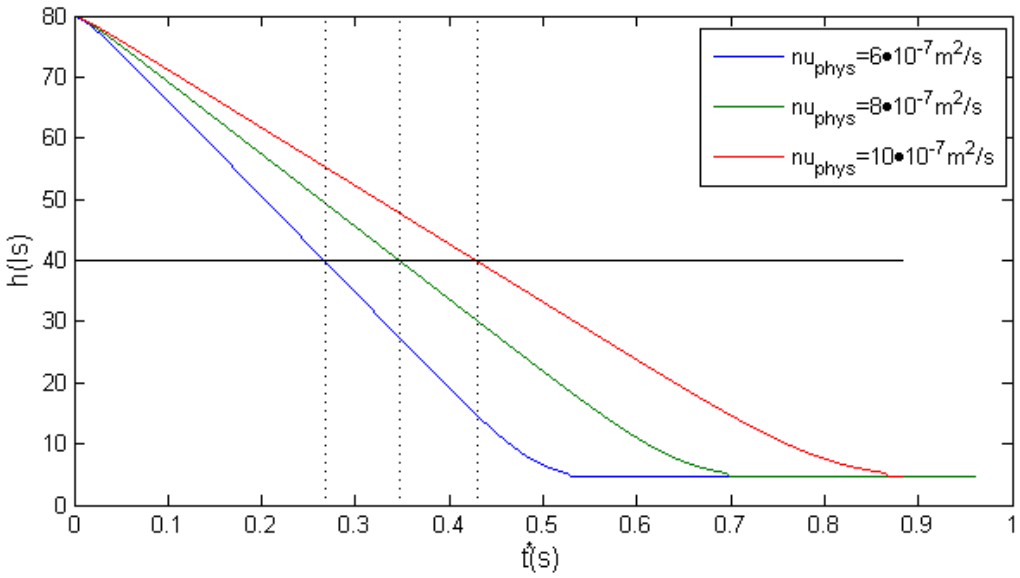

Figure 8. Three simulations for the $60 \times 60 \times 100\ \text{ls}^3$ grid and sphere with $\rho_s/\rho_l = 1.15$. The time each sphere took to reach $h_d = 40\text{ls}$ was recorded for further analysis. As T differs for each simulation t[lt] was converted to t^*[s].

When simulations with multiple values of ν^* are run, a data set is created combining a Δt_d with each value of ν^*. When plotted, like in Figure 9, these data resemble a $(\Delta t_d^*, \nu^*)$-calibration graph for the viscometer. If a certain Δt_d^* would be measured for the sphere to reach $h_d = 40\text{ls}$, these data points allow that information to be coupled to a certain viscosity. For example, if the sphere would reach the detection point in $\Delta t_d^* = 0.307\text{s}$, $\nu^* = 7.00\text{m}^2/\text{s}$ would be found, as can be seen in Figure 9.

The steepness of this graph is normative for the accuracy of the measurement device. This can be shown by direct conversion of a time measurement uncertainty to an uncertainty in the viscosity value, as the dotted lines in Figure 9 demonstrate. If $\Delta t_d^* = 0.307 \pm 0.01\text{s}$ was measured, this would result in an uncertainty range of $\nu^* = 7.00 \pm 0.25\text{m}^2/\text{s}$, or 7.14%. This method shows that a steeper graph will impose a less accurate determination of ν^*, because a certain interval on the Δt_d^* axis corresponds with a larger range on the ν^* axis.

Note that relatively large steps in ν^* were chosen in Figure 9. Interpolation can be used to acquire the data between the found values of ν^*, or more points can be simulated to obtain more accurate results.

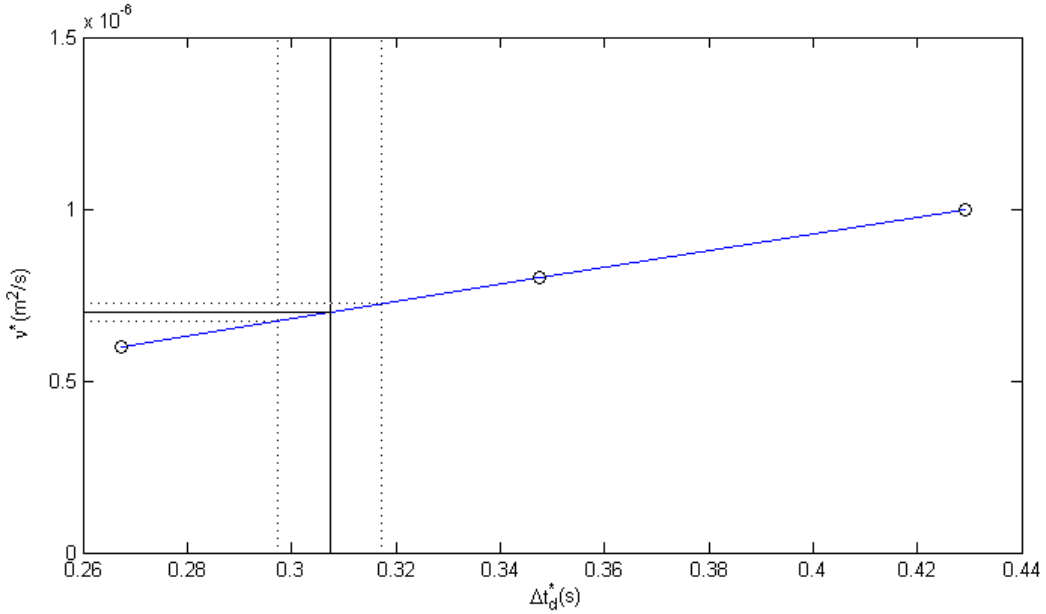

Figure 9. Calibration graph like data set. The intersections from Figure 8 are displayed as circles. An uncertainty conversion was made from Δt_d^* to ν^*.

When a feature of the model is changed, for example the density of the sphere, the steepness of the $\Delta t_d^*, \nu^*$-graph varies as well. By evaluating the steepness for either a higher or a lower density of the sphere, the effect of density variation on measurement accuracy can be researched.

3.3 Explored features of the viscometer

The effect of four properties on the measurement accuracy of a falling sphere viscometer were explored:

- The density ratio between the fluid and the sphere
- The cross sectional area of the vessel
- The shape of the settling object
- The height at which the object is detected

One data set was part of every property's analysis and therefore functions as a reference for each variated property. This set contains runs with the standard sphere with density ratio $\rho_s/\rho_l = 1.15$, with a 60×60 ls^2 cross sectional area and detection at $h_d = 40$ls.

3.3.1 Density ratio

For every simulation normalisation is applied on the particle densities, so that the fluid density in LBM remains constant in every dataset:

$$\rho_l = \sum_{i=1}^{Q} f_i = 1 \qquad (21)$$

Because the density ratio is defined to be ρ_s/ρ_l, the property of equation (21) causes the density ratio to be equal to the density of the sphere in the fluid. Even though the material of the sphere is cobalt, the density is still variable, as the core of the sphere may be hollow.

Densitie ratios ρ_s/ρ_l =1.05, ρ_s/ρ_l =1.15 and ρ_s/ρ_l =1.25 are examined. All simulations are done in the $60 \times 60 \times 100\text{ls}^3$ grid with the sphere-like shape, and the sphere is detected at $h_d = 40\text{ls}$.

3.3.2 Cross sectional area

The cross sectional area of the fluid volume is varied as well. The region where the largest velocity and pressure gradients occur, and thus where the grid must be fine, depends on the diameter of the sphere, D. As the sphere's diameter remains constant at $D = 9\text{ls}$, the fine grid, i.e. the center of a $16 \times 16 \times 100\ \text{ls}^3$, can be kept constant.

Therefore the volume of the coarse grid was changed so that total cross sectional areas of $40 \times 40\ \text{ls}^2$, $60 \times 60\ \text{ls}^2$ and $80 \times 80\ \text{ls}^2$ are created. Shear stress on the walls decelerates the sphere, so an in the cross sectional area decreases the wall effects, allowing the sphere have a larger velocity.

All simulations are done with $\rho_s/\rho_l = 1.15$ and the sphere, and detection occurs at $h_d = 40\text{ls}$.

3.3.3 Object shape

As stated in paragraph 3.3.1, the settling object is in most cases a point cloud, creating triangles that form a discretised sphere. The model has some constraints regarding the shapes it can process during the simulations: the shapes may not be concave, nor can the object have any sharp edges.

Therefore, a relatively conservative shape change was applied on the original sphere. It was slightly stretched in the z-direction to create egg-like shapes. To do so, the z coordinates of the point cloud were multiplied by factors 0.9, 1.0 and 1.1. This creates ellipsoids with various diameters: $D_x = D_y = D = 9\text{ls}$ for each object, and a varying $D_z = mD$, with $m = 0.9, 1.0, 1.1$.

Such a deformation affects the settling velocity in two ways. The volume, and thereby the mass, of the ellipsoids differs from that of the sphere. Furthermore, the changed shape and surface area both affect the drag. These deviations alternately accelerate and decelerate the sphere.

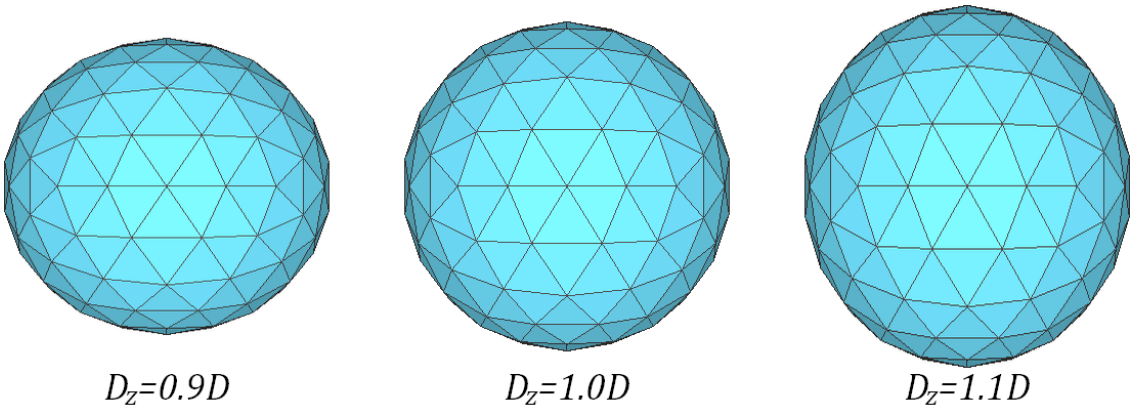

Figure 10. Three discretised objects. The one in the center represents an actual sphere. For the others the z coordinates were multiplied by 0.9 (left) and 1.1 (right).

Previously, to match the surface area of a real sphere better, a geometrical diameter, $D_{geom} = 9.16$, was applied on the discrete spheres that is used in all other simulations. Now ellipsoids are introduced, D_{geom} must be re-evaluated. However, the same rate of extension is a good approximation for the ellipsoids, as the number of facets remains the same and the diameters do not change much. In the model D_{geom} is applied as a factor D_{geom}/D which all coordinates are multiplied by. Therefore the D_{geom} part of the code remains the same for the ellipsoids.

The hydraulic diameter D_{hydr} must be adapted though. In the model, the hydraulic diameter is used to calculate the volume of a sphere with, i.e. $\pi D_{hydr}^3/6$. As explained in paragraph 2.5, D_{hydr} depends on ν. For the normal sphere, Rohde's [26] value of $D_{hydr} = 9.027\text{ls}$ can be used, as that value corresponds to $\nu = 1/6\text{ls}^2/\text{lt}$, which is close to $\nu = 0.19\text{ls}^2/\text{lt}$ that is used in this thesis. To calculate the volume of the ellipsoids, D_{hydr} was multiplied by the cube root of the multiplication factors 0.9 and 1.1.

All simulations are done in the $60 \times 60 \times 100\ \text{ls}^3$ volume with $\rho_s/\rho_l = 1.05\text{ls}$, and the sphere is detected at $h_d = 40\text{ls}$.

3.3.4 Detection height

Lastly, the detection height h_d was varied. Detection heights were 30ls, 40ls and 50ls. All simulations were done on the $60 \times 60 \times 100\ \text{ls}^3$ grid with the sphere while $\rho_s/\rho_l = 1.05\text{ls}$.

4 Results

4.1 Uncertainty variation caused by changing the density ratio

The $\Delta t_d^*, v^*$ graph of the density ratio (obtained like Figure 9) is shown in Figure 11. This figure is a graphical representation of measurement accuracy, as explained paragraph 3.2.2. The local steepness of the graph determines the accuracy, as a steeper graph results in a larger uncertainty in v^* when a certain measurement uncertainty range is applied on Δt_d^*. In Figure 11 two features stand out immediately. Firstly, the graph of $\rho_s/\rho_l = 1.05$ lies quite far from the other two, and secondly the graphs appear to be linear.

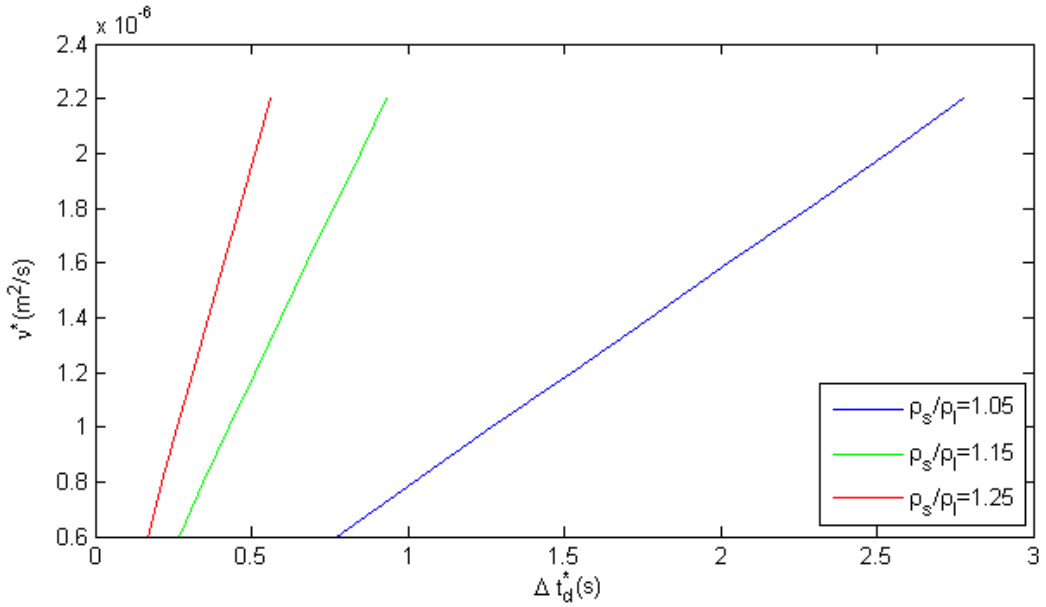

Figure 11. Each graph represents the time Δt_d^* in which the sphere reaches detection height $h_d = 40$ls for various viscosities. The density ratio between the sphere and the fluid is varied, creating three graphs. As the density ratio increases, the sphere moves faster, resulting in smaller Δt_d^* and steeper graphs.

Firstly, apparently the density ratio has an increasing impact on the settling time as it approaches $\rho_s/\rho_l = 1$. A longer Δt_d^* means that the velocity of the sphere becomes smaller. This relation is a logical result, as can be seen when the simulations are compared with the ideal case of a sphere that moves with constant velocity in an infinite volume. Equation 22 is the force balance of that ideal case, showing that v^* must grow when $\Delta\rho^* = \rho_s^* - \rho_l^*$ increases. Furthermore, C_D^* represents the drag coefficient, $A_\perp^*$ is the area perpendicular to the flow and V^* is the sphere's volume.

$$\frac{1}{2} C_D^* A_\perp^* \rho_l^* v^{*2} = V^* \Delta\rho^* |\vec{g}^*| \qquad (22)$$

Secondly, a statement about straightness can be reviewed by taking the derivative over Δt_d^*. Figure 12 shows the derivatives of each graph and makes clear that in case of a small density ratio the graph of Figure 11 indeed approaches a straight line, as the derivative is nearly constant. A constant derivative means that the accuracy of measurements is independent of which Δt_d^*, or v^*, is to be found.

A constant derivative indicates that the simulation resembles the settling trajectory of a sphere with a constant velocity in an infinite volume in case of Stokes flow. In the case of Stokes flow, $C_D^* \sim 1/\mathrm{Re}^*$ and $\mathrm{Re}^* = v^* L^*/\nu^*$, where L^* represents the characteristic length. Furthermore, $v^* = (L_z^* - h_d^*)/\Delta t_m^*$. Now the force balance (22) of a sphere with constant velocity in an infinite medium can be rewritten:

$$\frac{\nu^*}{\Delta t_d^*} \sim \frac{2V^* \Delta\rho^* |\vec{g}^*| L^*}{\rho_l^* A_\perp^* (L_z^* - h_d^*)} \qquad (23)$$

As each of the quantities at the right side of the equation are constant during the measurement, in the ideal case, $\nu^*/\Delta t_d^*$ would be constant over time. Apparently, the graph for $\rho_s/\rho_l = 1.05$ is a close approximation of the ideal case.

On the other hand, the curved left parts of the trends of larger density ratios show that the simulations do not mimic the ideal situation. Apparently, Δt_d^* dependence of the uncertainty occurs for measurements of smaller viscosities. Moreover, when the density ratio rises, the curvature of the graphs increases, so the measurement accuracy appears to be increasingly dependent of viscosity as the mass of the sphere increases. The increase in curvature is a result of non-ideal features of the model: the wall effect and acceleration trajectory.

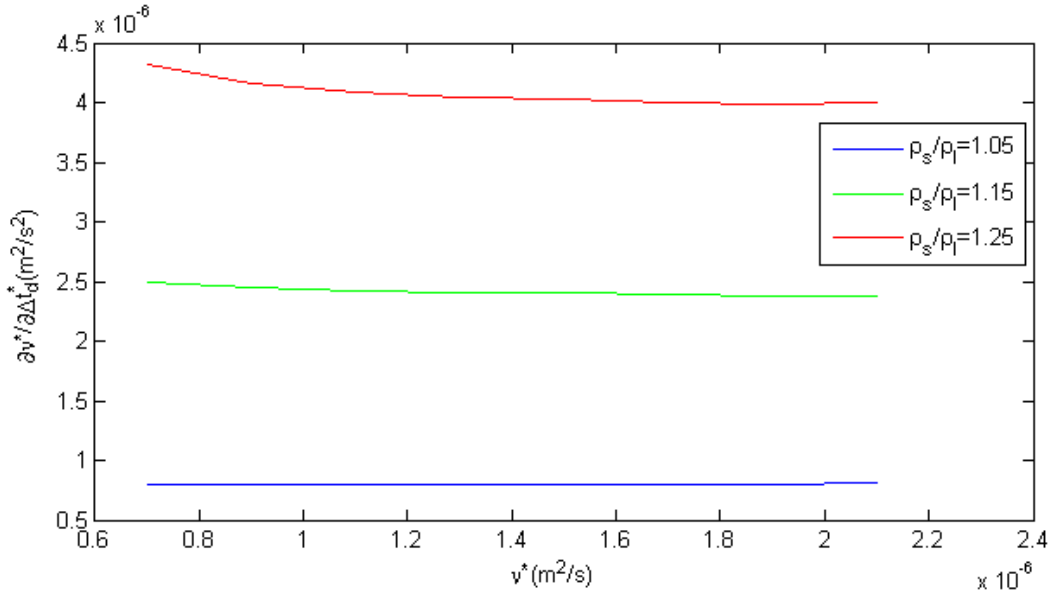

Figure 12. Derivative of ν^* over Δt_d^* of Figure 11. The steepness of the graphs of Figure 11 depends on both the density ratio ρ_s/ρ_l, as can be seen by the values of $\partial\nu^*/\partial\Delta t_d^*$, and on the viscosity ν^*, as the curvature of the graph shows. The curvature increases as the density ratio grows, causing the steeper graphs to become even steeper for small values of ν^*.

4.1.1 Accuracy assessment

In order to assess the three data sets equally regarding measurement accuracy, one value of ν^* is chosen. The Δt_d^* values of its intersections with the graphs are marked (Figure 13, for $\nu^* = 1.3 \cdot 10^{-6}\mathrm{m}^2/\mathrm{s}$). As every data set contains only nine measurements, interpolation is necessary to find these actual values of Δt_d^*. Due to the fact that all trends are quite straight, linear interpolation can be used.

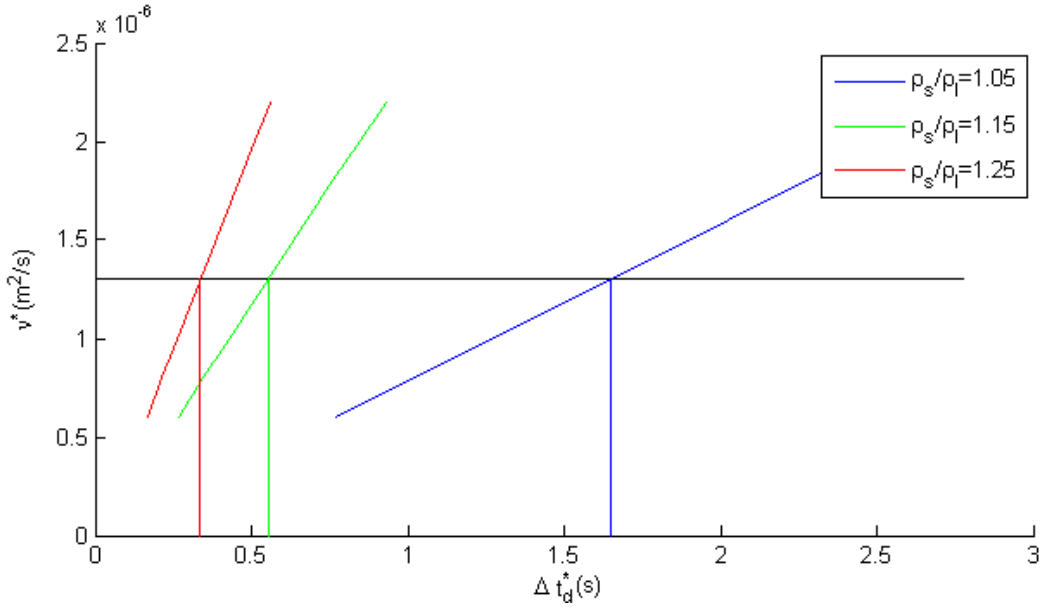

Figure 13. This figure resembles Figure 11, only a line representing $\nu^* = 1.3 \cdot 10^{-6}\mathrm{m}^2/\mathrm{s}$ is imposed. The intersections of the viscosity value and the three graphs mark the settling time Δt_d^* each sphere takes to reach the detection height $h_d = 40$ls.

Then a uncertainty range, $\pm\delta^*$, is applied to Δt_d^*, with $\delta^* = 0.01$s, as the time measurement device of the viscometer will have a measurement uncertainty. Then the points $\nu^*(\Delta t_d^* \pm \delta^*)$ are found, again by linear interpolation, as shown in the zoomed in Figure 14. The resulting uncertainty ranges are shown in Table 3.

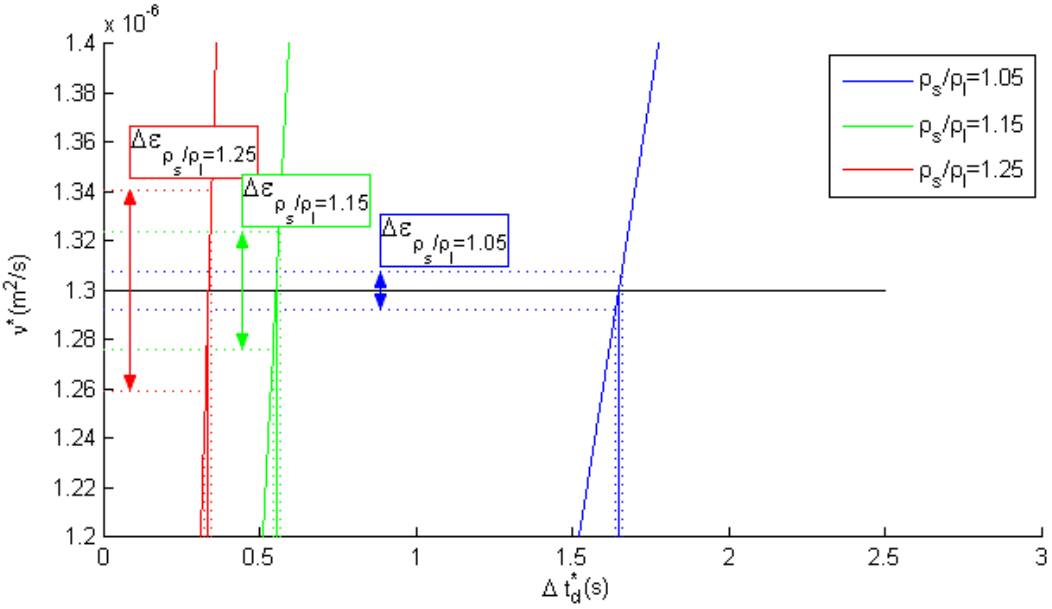

Figure 14. Zoomed in image of the intersections of Figure 13. A constant uncertainty range of 0.01s is imposed on the marked values of Δt_d^*. Each uncertainty range is translated to an uncertainty range in viscosity ν^*, that is marked by the coloured arrows. These values are shown in Table 3. The steeper the graphs are, the larger the found uncertainty becomes.

Table 3. Uncertainty assessment due to an uncertainty of $\delta = 0.01$ from Δt_d^* at $\nu^* = 1.3 \cdot 10^{-6}\mathrm{m}^2/\mathrm{s}$ for various density ratios.

ρ_s/ρ_l	1.05	1.15	1.25
Δt_d^*	1.649	0.554	0.335
$\nu^*(\Delta t_d^* + \boldsymbol{\delta}^*) \cdot 10^{-6}$	1.308	1.324	1.340
$\nu^*(\Delta t_d^* - \boldsymbol{\delta}^*) \cdot 10^{-6}$	1.292	1.276	1.260
$\Delta\nu^* \cdot 10^{-8}$	0.7914	2.402	4.044

The value of δ^* is arbitrarily chosen. The expected measurement uncertainty of the real viscometer is hard to predict, as it might appear difficult to measure Δt_d^* accurately in reality. The measurement would be the determination of the optimum of a passing magnetic field, which could be hard to do with great accuracy. However, as the simulated data lie in a quite straight line, linear interpolation is used. When points *a* and *d* are simulated data points and *b* and *c* represent points with x coordinates $\Delta t_d^* \pm \delta^*$ within that range of $[a\ b]$, then

$$\frac{\nu^*(d)-\nu^*(a)}{\Delta t_d^*(d)-\Delta t_d^*(a)} = \frac{\nu^*(c)-\nu^*(b)}{\Delta t_d^*(c)-\Delta t_d^*(b)} = \frac{\nu^*(c)-\nu^*(b)}{2\delta^*}$$

As long as *c* and *d* lie between points *a* and *b*, the uncertainty range $\varepsilon^* = \nu^*(c) - \nu^*(b)$ scales linearly with measurement uncertainty range $2\delta^*$, as the steepness is constant:

$$\nu^*(c) - \nu^*(b) = 2\delta^* C; \quad C = \frac{\nu^*(d)-\nu^*(a)}{\Delta t_d^*(d)-\Delta t_d^*(a)} \qquad (24)$$

Therefore, a smaller or larger value of δ^* would only result in an linear shift in the uncertainty range in ν^*. Thus, adjustments of δ^* add no further information when various simulations are to be compared.

This uncertainty analysis is repeated for the seven other values of ν^*. Table 4 shows the outcomes, expressed in both absolute uncertainty ranges ε^* $[\mathrm{m}^2/\mathrm{s}]$ and the uncertainty in terms of percent, $\varepsilon_{\%} = \varepsilon^*/\nu^*$. The data develop the same way as shown in Figure 12 because of the use of linear interpolation. The uncertainty is linearly correlated with the steepness of the graphs as shown in equation 24, and the course of that steepness is plotted in Figure 12.

The curvature of the graphs show that the uncertainty ranges increase for smaller values of ν^*. This effect depends on the density ration: the uncertainty rises significantly for the larger values of ρ_s/ρ_l, while the graph of $\rho_s/\ \rho_l = 1.05$ shows no curvature at all. Furthermore, the uncertainty ranges of smaller density ratios are significantly smaller.

The magnitude of the uncertainty ε^* for $\rho_s/\rho_l = 1.15$ lies roughly in the middle of those of the other density ratios. Figure 12 shows this: the distances between the middle graph and the other two are equal. This implies that the found uncertainty ranges scale linearly with the density ratios. This result can be predicted by analysis of the idealised version of the simulated setup: a sphere, settling with constant velocity in an infinite medium in the case of Stokes flow. The force balance was introduced in paragraph 4.1:

$$\frac{\nu^*}{\Delta t_d^*} \sim F\Delta\rho^*; \quad F = \frac{2V^*|\vec{g}^*|L^*}{\rho_l^* A_\perp^* (L_z^* - h_d^*)}$$

When $\Delta\rho^*$ is changed, this has a linear effect on the steepness of the graph. The same is shown in the simulations, where imperfections such as a non-constant velocity and wall effects create a small deviation from the statement of linearity.

Furthermore, the uncertainty ranges ε^* change hardly whereas as ν^* increases over various simulations. Therefore, $\varepsilon_{\%} = \varepsilon^*/\nu^*$ becomes smaller as the viscosity increases.

Lastly, the numerical instabilities in ε^* that appear in the otherwise constant part of the uncertainty ranges (i.e. the flat parts of the graphs in Figure 12) are analysed. For $\rho_s/\rho_l = 1.05$ the fluctuations are locked in a range of 2.5% of the mean uncertainty range $\bar{\varepsilon}^*$. Because the data set for $\rho_s/\rho_l = 1.05$ showed the relatively largest fluctuations, its 2.5% range supports the assumption that the deviations are due to the model's constraints and represent nothing physical.

Table 4. The uncertainty analysis of the three variations of density ratios. The uncertainty ranges ε^* and relative uncertainty ranges $\varepsilon_{\%}$ are significantly smaller for when ρ_s/ρ_l approaches 1. Furthermore, the relative uncertainty range decreases as ν^* increases.

	$\rho_s/\rho_l = 1.05$			$\rho_s/\rho_l = 1.15$			$\rho_s/\rho_l = 1.25$		
ν^* [m²/s] $\times 10^{-6}$	Δt_d^* [s]	ε^* [m²/s] $\times 10^{-9}$	$\varepsilon_{\%}$ [−]	t_d^* [s]	ε^* [m²/s] $\times 10^{-8}$	$\varepsilon_{\%}$ [−]	t_d^* [s]	ε^* [m²/s] $\times 10^{-8}$	$\varepsilon_{\%}$ [−]
0.7	0.896	8.03	1.1%	0.307	2.50	3.6%	0.190	4.31	6.2%
0.9	1.146	7.99	0.9%	0.388	2.44	2.7%	0.237	4.16	4.6%
1.1	1.397	7.94	0.7%	0.471	2.42	2.2%	0.286	4.09	3.7%
1.3	1.649	7.91	0.6%	0.554	2.40	1.8%	0.335	4.04	3.1%
1.5	1.901	7.96	0.5%	0.637	2.40	1.6%	0.385	4.02	2.7%
1.7	2.153	7.91	0.5%	0.720	2.40	1.4%	0.434	4.00	2.4%
1.9	2.405	7.94	0.4%	0.804	2.38	1.3%	0.484	3.99	2.1%
2.1	2.655	8.11	0.4%	0.888	2.38	1.1%	0.534	4.00	1.9%

4.2 Accuracy variation caused by changing the cross sectional area

Variation of the cross sectional area, of the cuboid was simulated next. From Figure 15 it immediately comes forward that the settling time increases as the area decreases. In case of a small area, wall effects have a larger decelerating effect on the sphere's velocity. The decrease of velocity translates to a less steep graph.

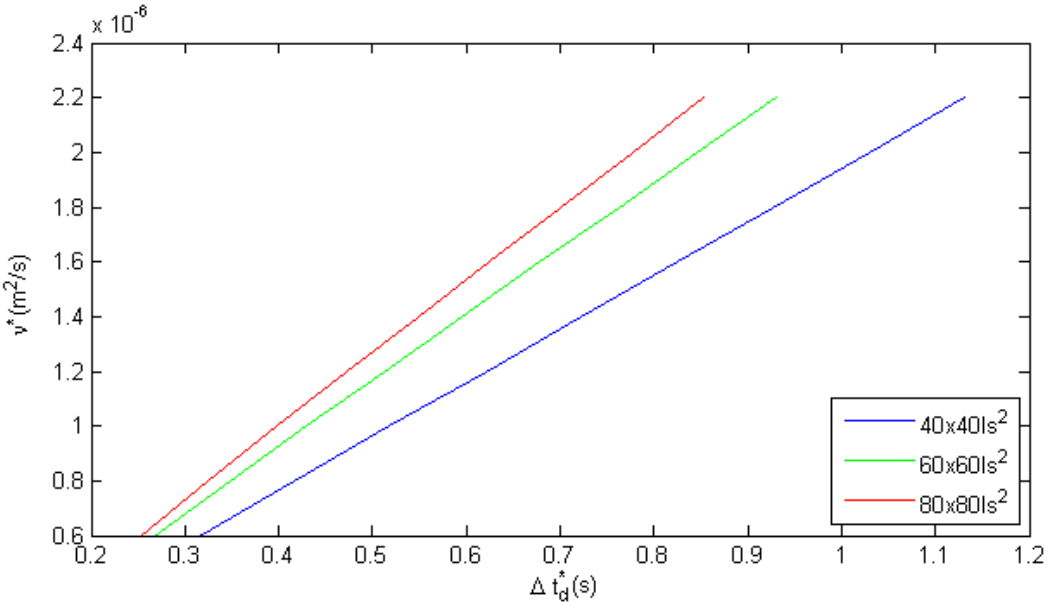

Figure 15. Each graph represents the time Δt_d^* in which the sphere reaches detection height $h_d = 40$ls for various viscosities. The cross sectional area is varied, which changes the wall effect on the settling sphere, creating three graphs. As the area decreases, the sphere is able to move faster, resulting in smaller Δt_d^* and steeper graphs.

Like in the case of the varied density ratios the trends seem linear. This is checked by taking the derivatives, that are shown in Figure 16. The curvature increases as the cross sectional area increases, so for smaller viscosities the $\Delta t_d^*, \nu^*$ graphs become steeper. Lastly, the bottom graph of Figure 16 again shows some numerical instabilities.

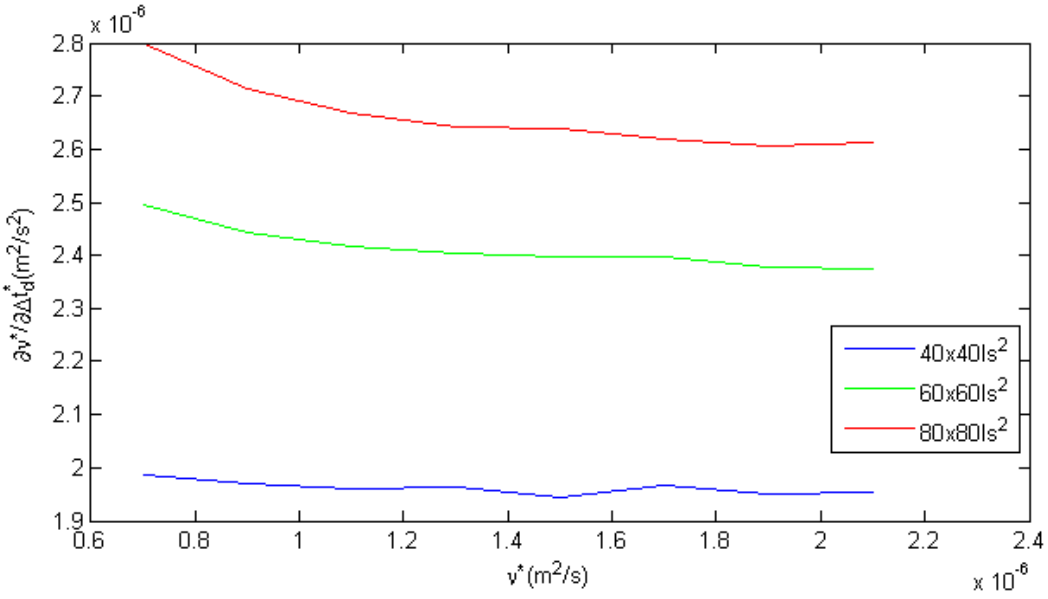

Figure 16. Derivative of ν^* over Δt_d^* of Figure 15. The steepness of the graphs of Figure 15 depends on both the applied cross sectional area, as can be seen by the values of $\partial \nu^* / \partial \Delta t_d^*$, and on the viscosity ν^*, as the curvature of the graph shows. The curvature increases as the density ratio grows, causing the steeper graphs to become even steeper for small values of ν^*.

4.2.1 Accuracy assessment

A measurement uncertainty of $\delta = \pm 0.01\text{s}$ is applied on the intersection values of Δt_d^* for $\nu^* = 1.3 \cdot 10^{-6}\text{m}^2/\text{s}$. Figure 16 shows that the uncertainties are dependent on the cross sectional area and that the smaller areas show smaller values of ε^*, as those produce the least steep graphs. However, the steepness of each of the three graphs appears to be approximately the same, resulting in smaller differences in ε^*.

The result of uncertainty analyses for multiple viscosities is shown in Table 5, and due to the linear interpolation method, the data scale linearly with Figure 16. The graphs show that the uncertainty ε^* increases as smaller values for ν^* are measured. The data also reveal that the significance of this local increase rises as the area becomes larger.

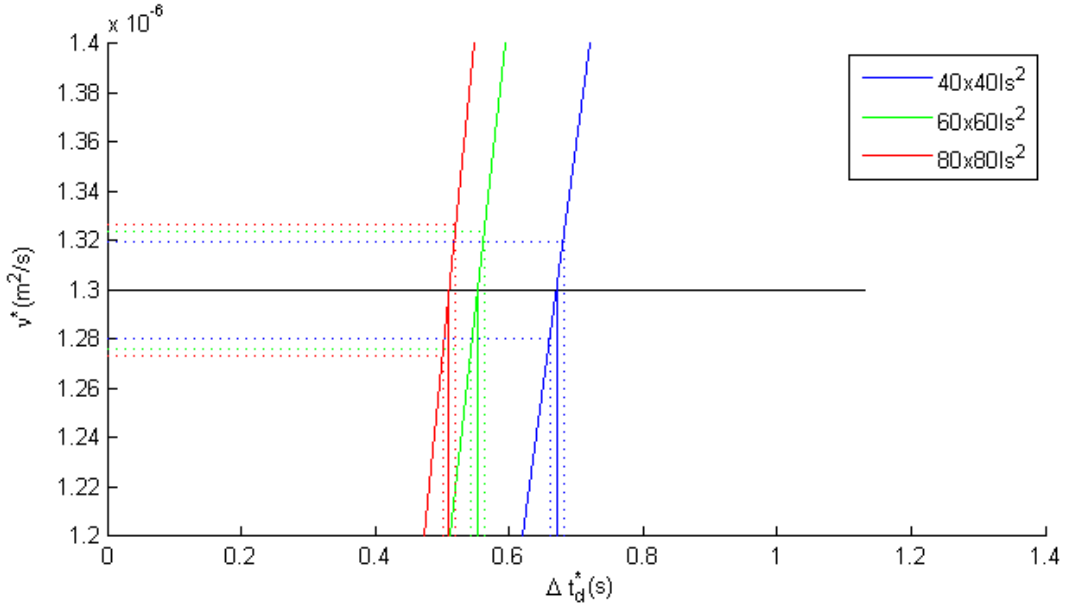

Figure 17. Zoomed in image of Figure 15 the intersections with $\nu^* = 1.3 \cdot 10^{-6}\text{m}^2/\text{s}$. A constant uncertainty range of 0.01s is imposed on the marked values of Δt_d^*. Each range is translated to an uncertainty range in viscosity ν^*, that is shown in the fourth row in Table 5. The steeper the graphs are, the larger the found uncertainty becomes.

The uncertainty ε^* generally increases as the area becomes larger, which is not promising because the simulated viscometer ultimately must measure in a vessel that is much larger than $1.2 \times 1.2 \times 2.0\ \text{mm}^3$. However, the uncertainty growth is a decreasing effect: $\varepsilon^*_{40\times40} - \varepsilon^*_{60\times60} < \varepsilon^*_{60\times60} - \varepsilon^*_{80\times80}$, and $\varepsilon^*_{80\times80} - \varepsilon^*_{100\times100}$ will again be smaller. The uncertainty ε^* will not grow along with dimension, but will hit an upper limit.

Table 5. The uncertainty analysis of the three variations of cross sectional areas. The uncertainty ranges ε^* and relative uncertainty ranges $\varepsilon_{\%}$ decrease for smaller cross sectional areas. Furthermore, the relative uncertainty range decreases as ν^* increases.

	$A = 40 \times 40\text{ls}^2$			$A = 60 \times 60\text{ls}^2$			$A = 80 \times 80\text{ls}^2$		
ν^* [m²/s] $\times 10^{-6}$	Δt_d^* [s]	ε^* [m²/s] $\times 10^{-8}$	$\varepsilon_{\%}$ [−]	t_d^* [s]	ε^* [m²/s] $\times 10^{-8}$	$\varepsilon_{\%}$ [−]	t_d^* [s]	ε^* [m²/s] $\times 10^{-8}$	$\varepsilon_{\%}$ [−]
0.7	0.366	1.99	2.8%	0.307	2.50	3.6%	0.288	2.80	4.0%
0.9	0.467	1.97	2.2%	0.388	2.44	2.7%	0.361	2.71	3.0%
1.1	0.569	1.96	1.8%	0.471	2.42	2.2%	0.435	2.67	2.4%
1.3	0.671	1.96	1.5%	0.554	2.40	1.8%	0.510	2.64	2.0%
1.5	0.773	1.94	1.3%	0.637	2.40	1.6%	0.586	2.64	1.8%
1.7	0.876	1.97	1.2%	0.720	2.40	1.4%	0.662	2.62	1.5%
1.9	0.978	1.95	1.0%	0.804	2.38	1.3%	0.739	2.61	1.4%
2.1	1.080	1.95	0.9%	0.888	2.38	1.1%	0.815	2.61	1.2%

4.3 Uncertainty variation caused by object deformation

Figure 18 clearly shows the resemblance between all three graphs. Apparently an elongation or compression of the sphere to $D_z = 1.1D$ or $D_z = 0.9D$ respectively has a much smaller effect than variations in the density ratio and area from the previous paragraph. This is of course partially due to the fact that relatively small deformations were chosen.

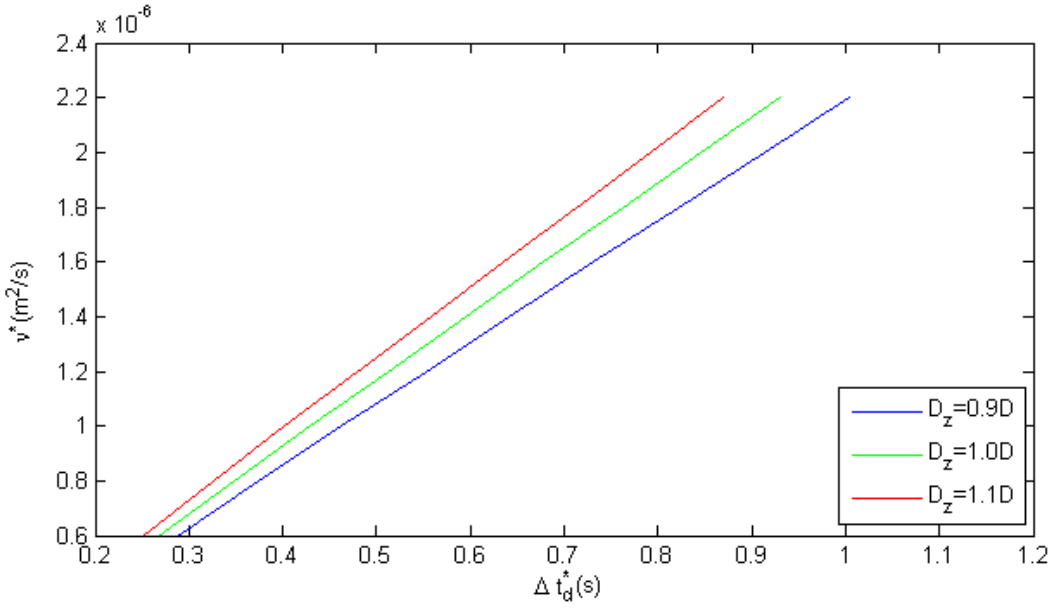

Figure 18. Each graph represents the time Δt_d^* in which the object reaches detection height $h_d = 40\text{ls}$ for various viscosities. The settling objects are a sphere's elongation in the settling direction, a normal sphere and a compressed sphere. As the diameter in the z direction, D_z, increases, the sphere is able to move faster, resulting in smaller Δt_d^* and steeper graphs.

However, it immediately becomes clear that the elongated sphere moves quicker than the compressed version. The effects of elongation are a 10% volume increase, which accelerates the sphere, but the increased volume also creates a larger surface area for shear stress to

work on, which decelerates it. The increased surface area will cause the object to experience more drag. However, apparently the accelerating due to mass affects the sphere more, as the elongated sphere settles faster.

$$\frac{1}{2} C_D^* A_\perp^* \rho_l^* v^{*2} = V^* \Delta\rho^* |\vec{g}^*| \qquad (22)$$

Lastly, with the graphs being closely together, the derivative of the graphs show small differences as well. Still, a slight decrease in the curvature can be noted when D_z decreases. This is shown in Figure 19.

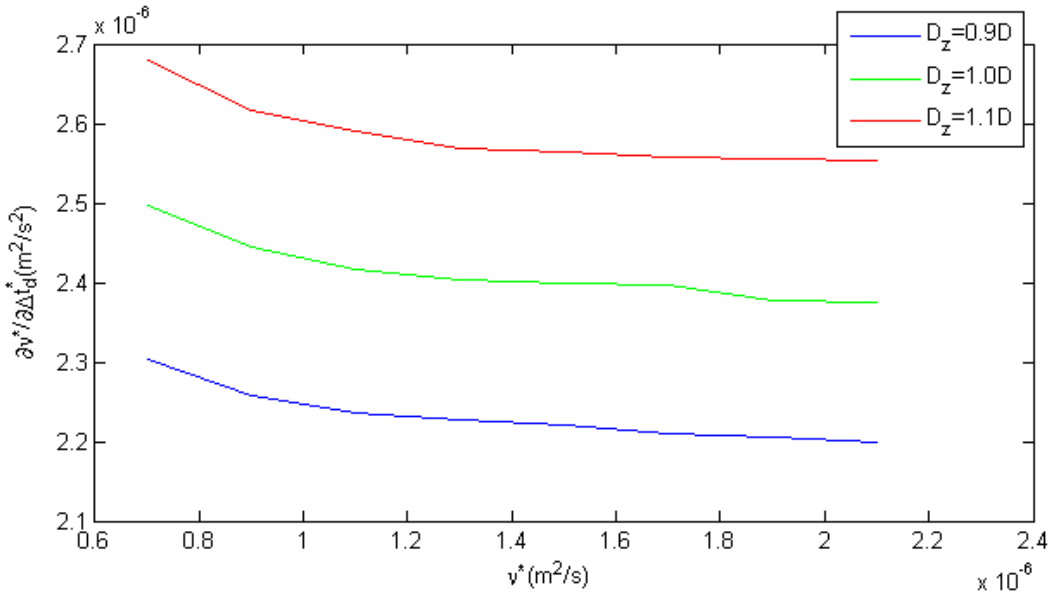

Figure 19. Derivative of v^* over Δt_d^* of Figure 18. The steepness of the graphs of Figure 18 depends on both the diameter in the z direction, D_z, as can be seen by the values of $\partial v^*/\partial \Delta t_d^*$, and on the viscosity v^*, as the curvature of the graph shows. The curvature is roughly equal for all graphs.

4.3.1 Accuracy assessment

Table 6 shows that when the length of the object increases, the uncertainty increases as well, as the object reaches a higher velocity and creates a steeper $(\Delta t_d^*, v^*)$ graph. The increase of the uncertainty scales almost linearly with the elongation, as the uncertainty range of the $D_z = 1.0D$ data set is nearly the mean of the other two sets.

The slight decrease in curvature as D_z becomes smaller, shown in Figure 19, which translates to a decrease in uncertainty range dependency of v^*.

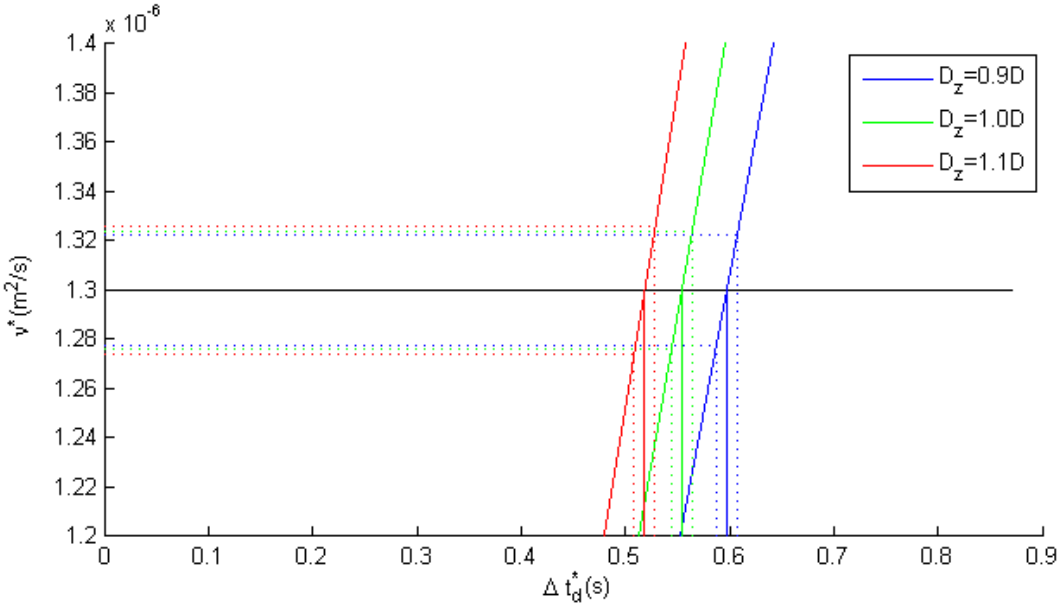

Figure 20. Zoomed in image of Figure 18 near the intersections with $\nu^* = 1.3 \cdot 10^{-6}\mathrm{m}^2/\mathrm{s}$. A constant uncertainty range of 0.01s is imposed on the marked values of Δt_d^*. Each range is translated to an uncertainty range in viscosity ν^*, that is shown in the fourth row in Table 6. The steeper the graphs are, the larger the found uncertainties becomes.

Table 6. The uncertainty analysis of the three variations of sphere deformations. The uncertainty ranges ε^* and relative uncertainty ranges $\varepsilon_{\%}$ of the varied D_z do not differ much, however, the uncertainty is smallest for $D_z = 0.9D$. Furthermore, the relative uncertainty range decreases as ν^* increases.

	$D_z = 0.9D$			$D_z = 1.0D$			$D_z = 1.1D$		
ν^* [m^2/s] $\times 10^{-6}$	Δt_d^* [s]	ε^* [m^2/s] $\times 10^{-8}$	$\varepsilon_{\%}$ [−]	t_d^* [s]	ε^* [m^2/s] $\times 10^{-8}$	$\varepsilon_{\%}$ [−]	t_d^* [s]	ε^* [m^2/s] $\times 10^{-8}$	$\varepsilon_{\%}$ [−]
0.7	0.33	2.30	3.3%	0.31	2.50	3.6%	0.29	2.68	3.8%
0.9	0.42	2.26	2.5%	0.39	2.44	2.7%	0.36	2.62	2.9%
1.1	0.51	2.24	2.0%	0.47	2.42	2.2%	0.44	2.59	2.4%
1.3	0.60	2.23	1.7%	0.55	2.40	1.8%	0.52	2.57	2.0%
1.5	0.69	2.22	1.5%	0.64	2.40	1.6%	0.60	2.56	1.7%
1.7	0.78	2.21	1.3%	0.72	2.40	1.4%	0.67	2.56	1.5%
1.9	0.87	2.21	1.2%	0.80	2.38	1.3%	0.75	2.56	1.3%
2.1	0.96	2.20	1.0%	0.89	2.38	1.1%	0.83	2.55	1.2%

4.4 Uncertainty variation caused by changing the detection height

Finally the height of the detection point was varied. The $(\Delta t_d^*, \nu^*)$ graph shows that settling time increases as the detection height becomes smaller, which is obvious because the distance the sphere must move increases.

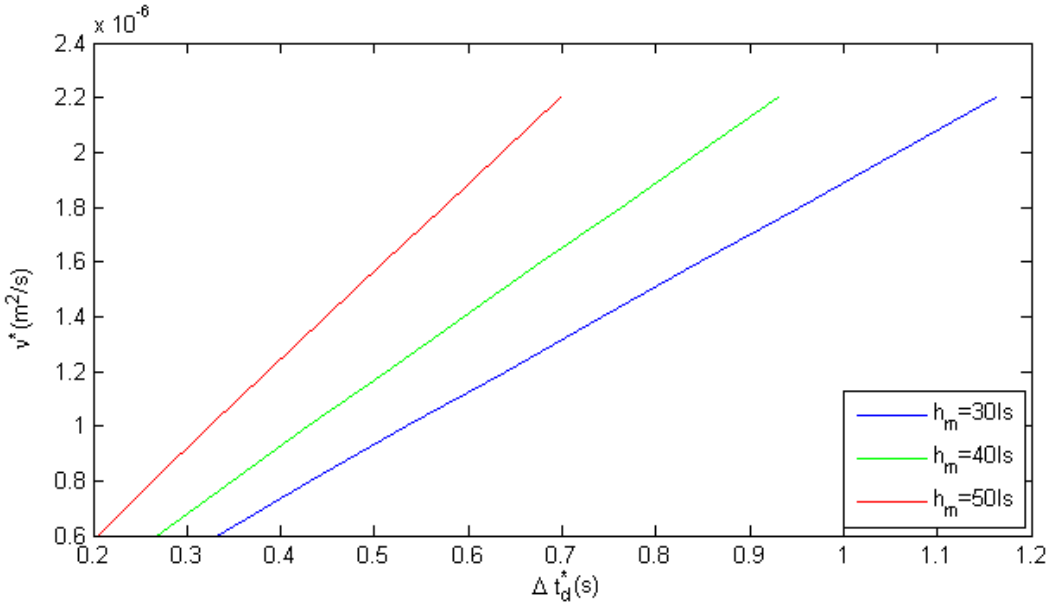

Figure 21. Each graph represents the time Δt_d^* in which the sphere reaches detection height $h_d = 40$ls for various viscosities. For each graph the height of the detection point, h_d, was varied. As the detection point gets further away from the bottom of the vessel, the time the sphere settles decreases, resulting in smaller Δt_d^* and steeper graphs.

What is remarkable about Figure 21 is how equal the distances are between the graphs that represent $h_d = 30$ls and $h_d = 40$ls and between $h_d = 40$ls and $h_d = 50$ls. The distances would be perfectly equal when the velocities of the spheres were constant over time. Apparently only a small effect deviates the graphs from having equal distances from each other.

The steepnesses in Figure 22 do not show equal distances between $h_d = 30$ls and $h_d = 40$ls and $h_d = 40$ls and $h_d = 50$ls. However, equal distances are expected in the ideal case, as is shown in the equation below, that represents the case of a sphere with constant velocity in an infinite medium with Stokes flow:

$$\frac{\nu^*}{\Delta t_d^*} \sim G(L_z^* - h_d^*); \quad G = \frac{2V^* \Delta\rho^* |\vec{g}^*| L^*}{\rho_l^* A_\perp^*}$$

If this equation represented the simulations of this paragraph, only h_d was to be varied. The fact that wall effects and acceleration are the same for every h_d-varying simulation means that the effect of a h_d variation from the equation should translate linearly to the simulation's outcome, so the steepnesses for h_m values that lie 10ls apart from $h_m = 40$ls, should show equal deviations from $(\partial \nu^* / \partial \Delta t_d^*)_{h_m = 40\text{ls}}$ as well.

However, the variable effect of the acceleration at the beginning of the trajectory creates an offset. The influence of that relatively slow part of the trajectory becomes smaller Δt_d^* increases. The deceleration near the bottom, which will appear most notable in case of $h_d = 30$ls, may affect this as well. The deceleration occurs near $h = 35$ls for every simulation, but the velocity loss is near 1% at $h = 30$ls, so the slowing effect remains nearly insignificant. However, these effects cause the distances between the three graphs to be unequal.

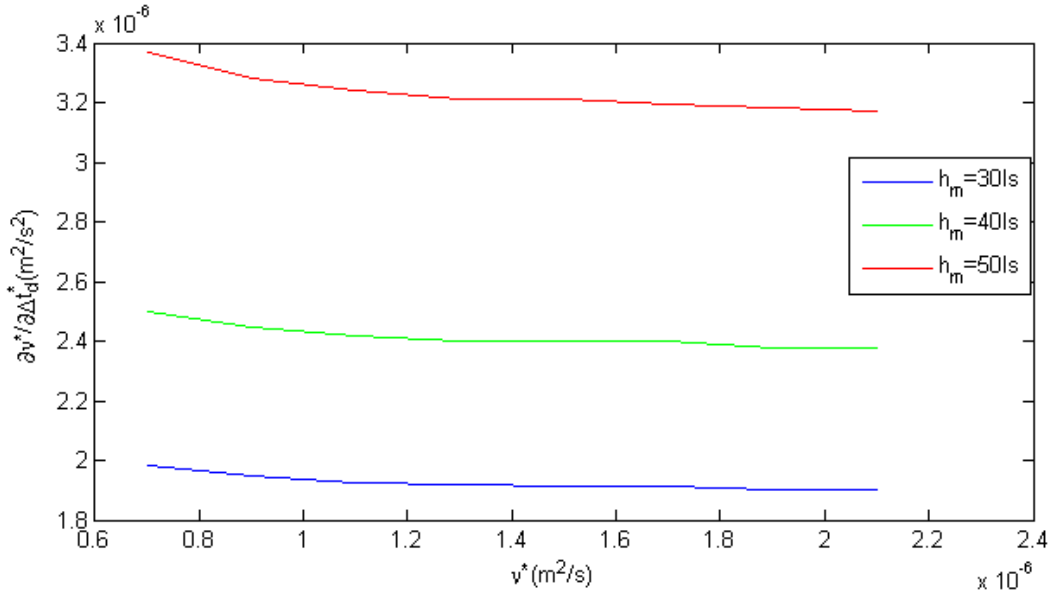

Figure 22. Derivative of ν^* over Δt_d^* of Figure 21. The steepness of the graphs of Figure 21 depends on both the detection height, as can be seen by the values of $\partial\nu^*/\partial\Delta t_d^*$, and on the viscosity ν^*, as the curvature of the graph shows. The curvature increases as the sphere is allowed less time to settle, causing the steeper graphs to become even steeper for small values of ν^*.

Lastly, Figure 22 shows that $\partial\nu^*/\partial\Delta t_d^*$ is hardly dependent on the detection height h_m, which is different from the previous results. The relatively large uncertainty for smaller velocities however, appears in this case like in all other cases.

4.4.1 Accuracy assessment

As shown in Figure 23, the uncertainty increases when detection occurs at a higher point, but not much. Table 7 shows that for lower viscosities, the uncertainty becomes larger, and this effect is nearly equal for every value of h_d.

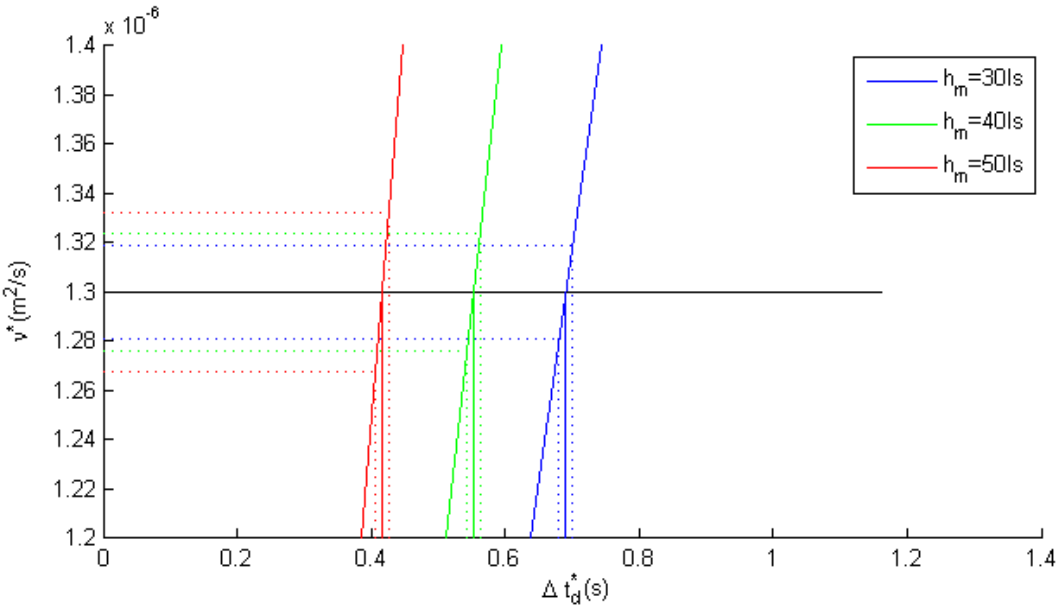

Figure 23. Zoomed in image of Figure 20 near the intersections with $\nu^* = 1.3 \cdot 10^{-6}\mathrm{m}^2/\mathrm{s}$. A constant uncertainty range of 0.01s is imposed on the marked values of Δt_d^*. Each range is translated to an uncertainty range in viscosity ν^*, that is shown in the fourth row in Table 7. The steeper the graphs are, the larger the uncertainty range becomes.

Table 7. The uncertainty analysis of the three variations of detection height. The uncertainty ranges ε^* and relative uncertainty ranges $\varepsilon_{\%}$ decrease as the detection height approaches the bottom. Furthermore, the relative uncertainty range decreases as ν^* increases.

	$h_d = 30$ls			$h_d = 40$ls			$h_d = 50$ls		
ν^* [m^2/s] $\times 10^{-6}$	Δt_d^* [s]	ε^* [m^2/s] $\times 10^{-8}$	$\varepsilon_{\%}$ [−]	t_d^* [s]	ε^* [m^2/s] $\times 10^{-8}$	$\varepsilon_{\%}$ [−]	t_d^* [s]	ε^* [m^2/s] $\times 10^{-8}$	$\varepsilon_{\%}$ [−]
0.7	0.381	1.98	2.8%	0.307	2.50	3.6%	0.233	3.37	4.8%
0.9	0.483	1.95	2.2%	0.388	2.44	2.7%	0.294	3.28	3.6%
1.1	0.587	1.93	1.8%	0.471	2.42	2.2%	0.355	3.24	2.9%
1.3	0.691	1.92	1.5%	0.554	2.40	1.8%	0.417	3.21	2.5%
1.5	0.795	1.91	1.3%	0.637	2.40	1.6%	0.479	3.21	2.1%
1.7	0.899	1.92	1.1%	0.720	2.40	1.4%	0.542	3.20	1.9%
1.9	1.004	1.90	1.0%	0.804	2.38	1.3%	0.604	3.18	1.7%
2.1	1.109	1.90	0.9%	0.888	2.38	1.1%	0.667	3.17	1.5%

5 Conclusion

5.1 Qualitative conclusions

The general outcome of the analysis of the simulations is that any variation in density, cross sectional area, object shape or detection height that allows the object to move a shorter time before it is detected, decreases the accuracy of the measurement. A larger velocity decreases Δt_m and, therefore, $\nu^*/\Delta t_d$ becomes larger. This causes an uncertainty range $\boldsymbol{\delta}^*$ in Δt_d to translate into a larger range ε^* in ν^*.

Another result that comes out of every data set was that the absolute uncertainty range is larger for smaller viscosities. This effect appears to be stronger in case of variations that increased the sphere's velocity. In the ideal case of a sphere that moves in an infinite volume with constant speed, the uncertainty range would be the same for every velocity. The reason the simulated data differ from the idealised values are wall effects and acceleration, and sometimes deceleration near the bottom has a small share as well.

5.2 Quantitative conclusions

The results section shows the effect that multiple variations of density ratio, cross sectional area, object shape and detection height have on the uncertainty in viscosity measurements. The effect of various property variations can be compared as they all share a reference measurement that was done with an object with $D_z = 1.0D$, $\rho_s/\rho_l = 1.15$ with a cross sectional area of $60 \times 60\text{ls}^2$ and a detection height of 40ls. This reference data set showed uncertainty ranges 3.6% for $\nu^* = 0.7 \cdot 10^{-6}\text{m}^2/\text{s}$, down to 1.1% for $\nu^* = 2.1 \cdot 10^{-6}\text{m}^2/\text{s}$

Analysis of the effects of three variations of the density ratio between the sphere and the liquid show that for a time measurement uncertainty of $\boldsymbol{\delta}^* = 0.01\text{s}$, uncertainty ratios in viscosity measurements can be reduced to 1.1% for $\nu^* = 0.7 \cdot 10^{-6}\text{m}^2/\text{s}$, down to 0.4% for $\nu^* = 2.1 \cdot 10^{-6}\text{m}^2/\text{s}$. This reduction takes place when $\rho_s/\rho_l = 1.05$, so by differentiation of 0.10 from the density ratio of the reference simulation set. Reduction of 55% of the cross sectional area in which the viscometer operates causes a smaller uncertainty decrease than that of the density variation: 2.8% down to 0.9% respectively. Furthermore an elongation of 10% shows an even smaller decrease in uncertainty range of 3.3% to 1.0%. Lastly, letting the sphere settle 10ls further than the reference measurement imposes an uncertainty range of 2.8% to 0.9%. This range is equal to the uncertainties due to area reduction.

Of course the effectiveness of uncertainty reductions depends on the magnitude of the variation that is applied on a property. A much larger cross sectional area reduction probably causes the uncertainty range to reach below that of $\rho_s/\rho_l = 1.05$. Still, small density ratios are a more easily applicable method to drastically decrease the uncertainty range in viscosity measurements. The constraint for minimisation of the uncertainty range lies in the maximum time a measurement may take. Theoretically, the uncertainty can be reduced drastically when the density of the sphere is nearly equal to the density of the liquid. However, this would cause Δt_d^* to become infinitely long, so the minimum uncertainty range depends on the maximum allowed measurement time.

5.3 Relation to constant velocity in an infinite volume

For the density ratio and the shape variations, the uncertainty scaled nearly linearly with the variation of the value ρ_s/ρ_l. In the case of density ratio the variations were translatable to a change of a single quantity in the force balance for stationary movement through an infinite volume. This direct relation explains the linear dependency of the uncertainty on the density ratio ρ_s/ρ_l.

The shape variation however, affects multiple quantities of that infinite case and therefore seems less predictable. The shape shift consisted of an elongation only, which affected volume (and thus mass) and surface area of the object. The effect on multiple quantities cannot be prevented, because if the V is to be kept constant while D_z increases, $A_\perp$ decreases et cetera. However, apparently a linear balance of the changed quantities is established, creating a linear dependency on the variation.

The detection height is one of the quantities of the idealised force balance, but the uncertainty range did not show this linear dependency on variation of h_d. This inconsistency is due to the fact that this time the sphere's velocity is not varied by a change in a property, but the distance the sphere had to cover instead. Apparently, because the acceleration part has a decreasing influence when the detection occurs nearer to the bottom, imposing a lower detection height has a clear minimising effect on the uncertainty range.

The fourth varied property, the cross sectional area, stands out as it is not part of the force balance of the ideal case. Besides, the cross sectional area cannot be tweaked to improve the performance of the viscometer, as it is the area of the vessel the viscometer has to measure in. Generally, an increasing cross sectional area means a decrease of wall effects on the sphere, and the wall effects are dependent on the sphere's velocity. The outcomes show that the sphere accelerates decreasingly as the bottom's dimensions are increased, and therefore that the uncertainty decreasingly grows.

6 Outlook

Future possibilities for research on the viscometer for a MSFR are twofold: adjustments should be made on the used LBM model to resemble reality in a better way, and multiple features of the viscometer must be explored to confirm whether the settling sphere method can actually be used.

6.1 Adjustments to the LBM model

The model that was used in this thesis resembles a very idealised version of a settling object in a fluid vessel and thus needs additional features to represent reality in a better way.

First of all, in the used model only one degree of freedom was allowed for the sphere to have. In reality drag could cause it to rotate, thereby introducing a translational motion in x or y directions as well, or the translation might be caused by any other fluid flow in that way inside the core. The possibility to rotate the sphere should be implemented in the model to explore potential motions in every direction.

Either a way to prevent these motions or a correction for it in software should be developed to create a working viscometer. The first option is preferable, as without any guiding equipment the settling object would be able to travel through the whole vessel, making repetitive measurements impossible. Adding a rod like object to the model, that allows the object to slide down like a bead around it, will prevent any drifting. Such an addition would also carry possibilities to raise the sphere up for next measurements. However, the effect of friction between the rod and the sphere must be researched.

Furthermore, the current results show that a compressed sphere delivers more accurate measurements than normal or elongated spheres, as such a flatter shape moves more slowly. However, these shapes are more likely to create vertices in their tails as they settle, which may again blur the measurements.

Regarding the shape of the object further research should be done on the various effects that elongation has, as it remains unclear whether the found effects are the result of a larger mass of the object, the actual shape or a larger area on which shear stress applies.

Lastly, the effect of the detection height on the uncertainty might behave differently if h_d would be decreased further, as deceleration affects the measurement increasingly as the bottom is near the detection height. For the explored heights a lower detection height seemed to result in smaller uncertainty ranges, but this may change if the deceleration near the bottom plays a larger part in the trajectory.

6.2 Practical conditions for a settling sphere viscometer

The practical features of the viscometer in the MSFR form a source of challenges that lay beyond this thesis.

Firstly, many physical phenomena that would take place when the viscometer would be used in reality, are not taken into account. Natural convection has serious consequences for this viscometer, as it would create a flow upwards. This flow would of course disturb the motion

of a settling sphere. The potential of the settling sphere viscometer depends on possibilities to correct for this upward convection.

Due to natural convection a non-uniform distribution of temperature, and thereby of density and viscosity, would be imposed on the volume. This affects measurements as local viscosity could differ from the mean viscosity of the vessel. The significance of this problem should be explored as well.

The communication between sphere and measurement device has to be researched further as well. This thesis assumes that detection of the magnetic field of the settling object is possible. However, it was not assessed whether a magnetic field would penetrate the materials of which the core's wall are to be made of. Furthermore, though cobalt is a ferromagnetic element, its potential to form a strong permanent magnet are not confirmed. Besides, although the Curie temperature of cobalt lies well above that of the core, the high temperature would still cause a decrease in the magnetic field to occur over time. Therefore a requirement for a minimal life time of a magnetic field of predetermined strength would have to be made and met.

If this works, the accuracy of time measurement using this magnetic field should be assessed and possibly enhanced, to enable viscosity measurements that have an appropriate uncertainty range.

Lastly, the current model can only combine a value of the viscosity with a measured time when the density of the molten salt is known. The results of this thesis show that the density ratio between the fluid and the sphere has the largest effect on the settling time and the uncertainty range, so accurate value must be known. The possibility to do these measurements is vital for this method. Therefore a method for measuring density must be known to be possible for further development of the settling sphere viscometer.

Table of symbols

Symbol	Description	Unit
A^{ϕ}	Surface of facet ϕ	ls^2
B_i	Additional mass due to motion of a wall	-
$\vec{c}_i$	Lattice velocity in direction i	$\mathrm{ls\,lt}^{-1}$
c_s	Speed of sound in LBM	$\mathrm{ls\,lt}^{-1}$
c_s^*	Speed of sound	$\mathrm{m\,s}^{-1}$
D	Diameter of a sphere	ls
D_{geom}	Geometrical diameter of the settling object	ls
D_{hydr}	Hydraulic diameter of the settling object	ls
D_x, D_y, D_z	Diameters in x, y and z directions of a ellipsoid	ls
f_i	Local particle density distribution	-
f_i^{eq}, f_i^{neq}	Local equilibrium function, nonequilibrium function	-
$\vec{g}$	Body force in LBM	$\mathrm{ls\,lt}^{-2}$
$\vec{g}^*$	Body force	$\mathrm{m\,s}^{-2}$
h	Height/z coordinate	ls
h_0	Height at $t = 0$lt	ls
h_d	Detection height	ls
L_x, L_y, L_z	Dimensions in x, y and z directions	ls
n	Level of refinement in case of local refinement	-
$\vec{n}^{\phi}$	Normal vector of a facet of the settling object	-
P_i^{dist}, P_i^{undist}	Disturbed/undisturbed mass fraction	-
Q	Amount of directions a particle flow can go	-
Q_i	The mass reflected by a wall	-
S	Spatial scaling factor in LBM	mls^{-1}
T	Time scaling factor	$\mathrm{s\,lt}^{-1}$
$t_{f,i}$	Scaling factor depending on type of LBM	-
Δt	Discrete time step	lt
Δt_d^*	Time between release and detection	s
$\vec{u}_i$	Macroscopic velocity (in direction i)	$\mathrm{ls\,lt}^{-1}$
$\vec{u}^*$	Macroscopic velocity	m/s
U_{max}	Maximum velocity of Poiseuille flow profile	$\mathrm{ls\,lt}^{-1}$
v	Velocity of settling object in LBM	$\mathrm{ls\,lt}^{-1}$
v^*	Velocity of settling object	ms^{-1}
V_i^{ϕ}	Intersection volume	ls^3
ΔV	Volume of a boundary cell	ls^3
$\vec{x}$	Spatial position	ls
Δx	Discrete spatial step	ls
z_k	Height of boundary cell k	ls

Greek	Description	Unit
α	Area of a grid cell	ls^2
$\Gamma_i^{out,\phi}$	Mass reflected from facet ϕ	-
δ^*	Uncertainty in measured time	lt
ε^*	Uncertainty range in viscosity	$\mathrm{ls}^2\ \mathrm{lt}^{-1}$
$\varepsilon_{\%}^*$	Relative uncertainty range in viscosity	-
ν	Kinematic viscosity in LBM	$\mathrm{ls}^2\ \mathrm{lt}^{-1}$
ν^*	Kinematic viscosity	$\mathrm{m}^2\ \mathrm{s}^{-1}$
ρ_l, ρ_s	Density of liquid/object in LBM	ls^{-3}
ρ_l^*, ρ_s^*	Density of liquid/object	$\mathrm{kg\ m}^{-3}$
τ	Relaxation term	-
ϕ	Indication of a facet	-
Ψ_i^{ϕ}	Volume of parallelepiped	ls^3
Ω_i	Collision operator in direction *i*	-

Bibliography

[1] United Nations, Department of Economic and Social Affairs, Population Division, "World Population Prospects: The 2015 Revision, Key Findings and Advance Tables," ESA/P/WP.241, 2015.

[2] Z. Liu, Global Energy Interconnection, London: Elsevier, 2015.

[3] Nuclear Energy Agency (OECD), "Technology Roadmap Update for Generation IV Nuclear Energy Systems," 2014.

[4] E. Merle-Lucotte, *The concept of Fast Spectrum Molten Salt Reactor (MSFR),* French-Swedish Seminar on Future Nuclear Systems - KTH – Stockholm, Sweden.

[5] G. J. Janz and R. P. T. Tomkins, Physical Properties Data Compilations Relevant to Energy Storage:IV Molten Salts: Data on Additional Single and Multi-Component Salt Systems, National Bureau of Standards Report NSRDS-NBS 61 Part IV, 1981.

[6] A. Malkin and A. Isayev, Rheology: Concepts, Methods & Applications, Toronto: ChemTec Publishing, 2006.

[7] M. Rohde, *From personal communications,* 2015.

[8] M. Pajda, J. Kudrnovsky, I. Turek, V. Drchal and P. Bruno, "Ab initio calculations of exchange interactions, spin-wave stiffness constants, and Curie temperatures of Fe, Co, and Ni," *Physical Review B,* vol. 64, no. 17, p. 174402, 2001.

[9] J. Hardy, O. d. Pazzis and Y. Pomeau, "Molecular dynamics of a classical lattice gas: Transport properties and time correlation functions," *Physical Review A,* vol. 13, no. 5, pp. 1949-1961, 1976.

[10] U. Frisch, B. Hasslacher and Y. Pomeau, "Lattice-Gas Automata for the Navier-Stokes Equation," *Physical Review Letters,* vol. 56, no. 14, pp. 1505-1508, 1986.

[11] G. R. McNamara and G. Zanetti, "Use of the Boltzmann Equation to Simulate Lattice-Gas Automata," *Physical Review Letters,* vol. 61, no. 20, pp. 2332-2335, 1988.

[12] Y. H. Qian, D. d'Humières and P. Lallemand, "Lattice BGK Models for Navier-Stokes Equation," *Europhysics Letters,* vol. 17, no. 6, pp. 479-484, 1992.

[13] M. Rohde, J. J. Derksen and H. E. A. van den Akker, "Volumetric method for calculatring the flow around moving objects in lattice-Boltzmann schemes," *Physical Review E,* vol. 65, p. 056701, 2002.

[14] D. Kandhai, W. Soll, S. Chen, A. Hoekstra and P. Sloot, "Finite-Difference Lattice-BGK Methods on Nested Grids," *Computer Physics Communications,* vol. 129, no. 1-3, pp. 100-109, 2000.

[15] X. He, L.-S. Luo and M. Dembo, "Some progress in lattice Boltzmann method: part I: Nonuniform mesh grids," *Journal of Computational Physics,* vol. 129, no. 2, pp. 357-363, 1996.

[16] M. Rohde, D. Kandhai, J. J. Derksen and H. E. A. van den Akker, "A generic, mass conservative local grid refinement technique for lattice-Boltzmann schemes," *International Journal for Numerical Methods in Fluids,* vol. 51, no. 4, pp. 439-468, 2006.

[17] H. Brenner, "Dynamics of a particle in a viscous fluid," *Chemical Engineering Science,* vol. 17, no. 6, pp. 435-466, 1962.

[18] A. J. C. Ladd and R. Verberg, "Lattice-Boltzmann Simulations of Particle-Fluid Suspensions," *Journal of Statistical Physics,* vol. 104, no. 5, pp. 1191-1250, 2001.

[19] S. Chen and G. D. Doolen, "Lattice Boltzmann Method for Fluid Flows," *Annual Review Fluid Mechanics,* vol. 30, pp. 30:329-364, 1998.

[20] X. He, Q. Zhou, L. Luo and M. Dembo, "Analytic solutions and analysis on non-slip boundary conditions for the lattice-Boltzmann BGK model," *Journal of Statistical Physics,* vol. 87, no. 1, pp. 115-136, 1997.

[21] M. Rohde, D. Kandhai, J. J. Derksen and H. E. A. van den Akker, "Improved bounce-back methodes for no-slip walls in lattice-Boltzmann schemes: Theory and simulations," *Physics Review E,* vol. 67, p. 066703, 2003.

[22] P. J. Dellar, "Incompressible limits of lattice Boltzmann equations using multiple relaxation times," *Journal of Computational Physics,* vol. 190, no. 2, p. 351–370, 2003.

[23] B. Chopard, A. Dupuis, A. Masselot and P. Luthi, "Cellular automata and Lattice Boltzmann techniques: An approach to model and simulate complex systems," *Advances in Complex Systems,* vol. 5, no. 2, pp. 103-246, 2002.

[24] H. Chen, C. Teixeira and K. Molvig, "Realization fo fluid boundary conditions via discrete Boltzmann dynamics," *Int. J. Mod. Phys. C,* vol. 9, no. 8, p. 1281, 1998.

[25] H. Hasimoto, "On the periodic fundamental solutions of the Stokes equations and their application to viscous flow past a cubic array of spheres," *Journal of Fluid Mechanics,* vol. 5, no. 2, pp. 317-328, 1959.

[26] M. Rohde, J. J. Derksen and H. E. A. van den Akker, "An applicability study of advanced lattice-Boltzmann techniques," *Computers & Fluids,* vol. 37, no. 10, p. 1238–1252, 2008.

[27] A. ten Cate, C. H. Nieuwstad, J. J. Derksen and H. E. A. van den Akker, "Particle imaging velocimetry experiments and lattice-Boltzmann simulations on a single sphere settling under gravity," *Physics of Fluids,* vol. 14, no. 11, pp. 4012-4025, 2002.

[28] M. A. Sohal, M. A. Ebner, P. Sabharwall and P. Sharpe, Engineering Database of Liquid Salt Thermophysical and Thermochemical Properties, Idaho Falls: Idaho National Laboratory, 2010.